Maria Inês Santos Silva

Bachelor Degree in Mechanical Engineering Sciences

Non-Destructive Testing for Polymer Matrix Composites produced by Additive Manufacturing

Thesis to obtain the Master Degree in Mechanical Engineering

Supervisor: Doctor Telmo Jorge Gomes dos Santos, Associate Professor with Habilitation, NOVA School of Science and Technology
Co-Supervisor: Doctor Miguel Araújo Machado, Assistant Professor, NOVA School of Science and Technology

President: Doctor Carla Maria Moreira Machado
Examiner: Doctor Marta Isabel Pimenta Verdete da Silva Carvalho
Examiner: Doctor Luís Filipe Soldado Granadeiro Rosado
Supervisor: Doctor Telmo Jorge Gomes dos Santos

FACULDADE DE CIÊNCIAS E TECNOLOGIA
UNIVERSIDADE NOVA DE LISBOA

July 2020

Non-Destructive Testing for Polymer Matrix Composites produced by Additive Manufacturing

ACKNOWLEDGEMENTS

I would like to begin by thanking my master thesis supervisor, Professor Telmo Santos, for accepting me as his supervised student in the present research and for all his guidance and support during the past five years.

I also wish to thank Professor Miguel Machado, my master thesis co-supervisor, who also helped me get acquainted with this field of research and who has always shown availability and readiness to help me.

To the staff of the laboratories of the Mechanical Technology Group and to the master students and PhD students who have endlessly supported my work. A special mention to Tiago Rodrigues for all the help and advice given throughout the course.

To Professor João, who has inspired and helped me to pursue and achieve many of my academical deeds, and to Professor Carla Machado, for inviting me to assist one of the Mechanical and Industrial Engineering Department laboratories.

To Dr. Júlia Murta, for helping me realize that the solution to my problems lies within myself.

To Professor Pedro Vilaça and Professor Evgenii Malitckii, for accepting me as a researcher in their project and as their supervised PhD student.

To all the families I now belong to, through my volunteering work in organizations such as GASTagus and BEST Almada, that taught me the importance of interdependence and reciprocation, and that led me to a path of reinvention, of gratitude, empathy and inner growth.

To all my friends, and to those whom I came across during my journey. They all taught me something, among others, the importance of kindness, tolerance, and support for one another.

Above all, to my family and especially to my mother, my role model, who taught me the healing power of love, the true meaning of forgiveness and resiliency and the significance of having an inside-out approach in order to thrive and achieve peace of mind.

This work was funded by the Project POCI-01-0145-FEDER-016414 (FIBR3D), cofinanced by Programa Operacional Competitividade e Internacionalização and Programa Operacional Regional de Lisboa, through Fundo Europeu de Desenvolvimento Regional (FEDER) and by National Funds through Fundação para a Ciência e a Tecnologia (FCT-MCTES).

ABSTRACT

The increased use of composite materials produced by Additive Manufacturing (AM), in fields like automotive and aerospace, raises new demands in characterizing a variety of defects that may appear during its production and service life and which have an impact on the structural performance of the component. Conventional Non-destructive testing (NDT) cannot fulfil these new requirements, motivating the research and development of new, innovative approaches that increase the inspection reliability.

The purpose of this work is to apply and test the reliability of two innovative NDT techniques, Double Active Transient Thermography (DATT) and reflection mode Air-coupled Ultrasound (ACU), and its inspection parameters to evaluate polymer matrix composites produced by AM.

In the DATT experiments, the samples were excited by two heat sources, a cold flow and a heat flow, six different parameters were used (the instant for starting the cold flow and its duration, different defects and the influence of the lid, exposure time, curvature, and instant when the vortex is turned on) and the goal of developing this technique was to observe, with the same level of temperature contrast and at the same time, different defects at different depths and locations. In the ACU experiments, three parameters were studied (α, d and d_p), and the goal was to understand their effect in the reflection echo of the wave.

The DATT results are promising, allowing an increased understanding of the influence of each parameter and a clearer observation of the three defects with different locations and depths at the same time. The ACU results allow to understand the effect of the studied parameters but future improvements on equipment structure and assembly and the usage of different probes and samples will play a role in better understanding not only the wave's behaviour but also the advantages of the technique.

KEY-WORDS

Additive Manufacturing, Composites, Non-destructive Testing, Double Active Transient Thermography, Air-coupled Ultrasound, Defects

RESUMO

O crescente uso de materiais compósitos produzidos por Fabrico Aditivo (FA), em indústrias como a automóvel e a aeroespacial, criam novas exigências na deteção e caracterização de defeitos que possam surgir durante a produção ou tempo de vida destes materiais e que podem comprometer o desempenho do componente. Os Ensaios Não Destrutivos (END) convencionais apresentam algumas limitações na inspeção destes materiais, pelo que é necessário estudar e desenvolver novas técnicas que permitam aumentar a fiabilidade da inspeção.

O objetivo desta tese foi o de implementar e testar a fiabilidade de duas técnicas END inovadoras, *Double Active Transient Thermography* (DATT) e *Air-coupled Ultrasound* (ACU), e os seus parâmetros de inspeção na caraterização de compósitos de matriz polimérica produzidos por FA.

Nas experiências de DATT, os provetes foram expostos a duas fontes de calor, uma fonte fria e uma quente, foram estudados seis parâmetros diferentes (o instante em que começa o frio e a sua duração, diferentes defeitos e a influência da tampa, tempo de exposição, curvatura, e instante em que se liga o vortex) e o objetivo destes testes foi o de observar, com o mesmo nível de contraste térmico e ao mesmo tempo, diferentes defeitos com diferentes espessuras e localizações. Nas experiências de ACU, foram estudados três parâmetros diferentes (α, d and d_p), com o objetivo de compreender o seu efeito na onda refletida.

Os resultados de DATT são promissores e permitem uma melhor compreensão da influência de cada parâmetro e a observação dos vários defeitos ao mesmo tempo. Os resultados de ACU permitem compreender o efeito dos parâmetros, mas futuras melhorias na estrutura do equipamento e novos ensaios com diferentes sondas e diferentes provetes contribuirão para a compreensão do comportamento da onda e as vantagens da técnica.

PALAVRAS-CHAVE

Fabrico Aditivo, Compósitos, Ensaios Não Destrutivos, Double Active Transient Thermography, Air-coupled Ultrasound, Defeitos

CONTENTS

Acknowledgements v
Abstract vii
Key-words vii
Resumo ix
Palavras-chave ix
CONTENTS xi
List of figures xiii
List of tables xvii
Abbreviations xix
Symbols xx
1 – Introduction 1
1.1 – Motivation 1
1.2 – Goals 3
1.3 – Thesis Structure 4
2 – Literature review 5
2.1 – Introduction 5
2.2 – Polymer Matrix Composites 6
2.2.1 – Polymer Matrix 7
2.2.2 – Reinforcement Material 8
2.2.3 – Defects in PMC 9
2.3 – Additive Manufacturing 10
2.3.1 – Fused Filament Fabrication 10
2.3.2 - State-of-the-art of composites produced by AM 13
2.4 – Active Pulsed Thermography 14
2.4.1 – Properties and types of techniques 15
2.4.2 – Thermography data 18
2.4.3 – Limitations of IRT 18
2.4.4 - State-of-the-art of PT for Polymer Matrix Composites evaluation 19
2.5 – Air-Coupled Ultrasound 20
2.5.1 – Physics of Ultrasound 21
2.5.2 – Equipment and transducers 24
2.5.3 – Air-Coupled Ultrasound 25
2.5.4 – Data presentation 26
2.5.5 – Limitations of UT 26
2.5.6 - State-of-the-art of ACU for Polymer Matrix Composites evaluation 27
2.6 – Chapter resume and conclusions remarks 27
3 – Experimental Procedure 29
3.1 – Introduction 29

3.2 – DATT setup 29
3.3 – ACU equipment 31
3.4 – Sample One 33
3.5 – Sample Two 35
3.6 – Sample Three 36
3.7 – Sample Four 37
3.8 – Sample Five 37
3.9 – Chapter resume 38
4 – Results and discussion of DATT characterization tests 39
4.1 – Introduction 39
4.2 – Sample One (1P) inspection 40
4.2.1 – Group One 40
4.2.2 – Group Two 44
4.2.3 – Group Three 46
4.2.4 – Group Four 49
4.3 – Sample One (1C) inspection 51
4.4 – Cold flow experiment with air (Sample One) 54
4.4.1 – Group One 54
4.4.2 – Group Two 55
4.5 – Experiment with cooling fluid Regex G13 (Sample One) 56
4.6 – Sample Two inspection 58
4.7 – Chapter resume 60
5 – Results and discussion of ACU characterization tests 63
5.1 – Introduction 63
5.2 – ACU setup 63
5.3 – Sample Four inspection 65
5.3.1 – Group One 66
5.3.2 – Group Two 70
5.4 – Sample Three inspection 72
5.5 – Sample Five inspection 74
5.6 – Chapter resume 75
6 – Conclusions and suggestions for future works 77
6.1 – Conclusions 77
6.2 – Suggestions for future works 79
References 81
Appendix 89
Appendix 1. Common matrix materials and its properties 89
Appendix 2. Two modes of wave propagation in solids 90

LIST OF FIGURES

Figure 2.1 - Example of the structure of a fibre-reinforced composite. 7
Figure 2.2 - Examples of defects in PMC. 9
Figure 2.3 - Schematic representation of a typical FFF setup. 10
Figure 2.4 - Examples of FFF parameters. 12
Figure 2.5 - Example of defects found in FFF: a) voids b) 'staircase' effect c) warping. 13
Figure 2.6 - Schematic view of a pulsed thermography inspection. 17
Figure 2.7 - Reflection and transmission modes. 18
Figure 2.8 - Examples of IRT applications a) temperature distribution of plastics in injection moulds b) temperature distribution of composite materials. 18
Figure 2.9 - Schematic representation of a) refraction b) diffraction. 24
Figure 2.10 - Ultrasound system. 25
Figure 2.11 - Methods of testing a) transmission b) shear wave c) plate waves. 26
Figure 3.1 – DATT schematic experiment setup 30
Figure 3.2 – a) DATT setup with the vortex b) Meech Vortex Tube and sample c) DATT setup with the cooling fluid d) pouring the cooling fluid into the sample. 31
Figure 3.3 - ACU equipment a) real experiment set-up in reflection mode b) equipment used and sample c) schematic experiment set up. 32
Figure 3.4 - ACU equipment a) placement of the probes b) flaw detector. 33
Figure 3.5 - Sample One a) printed version b) model showing the delaminations with the legend of the defects and outer wall. 34
Figure 3.6 - Representation of the delaminations of plain side, regarding their depths and locations. 34
Figure 3.7 - Lid with one entrance for the cold flow 35
Figure 3.8 - Sample two a) printed model b) dimensions. 35
Figure 3.9 - Model of Sample two displaying the a) depth and b) position of each defect. 36
Figure 3.10 - Sample three a) dimensions b) model displaying the delamination. 37
Figure 3.11 - Sample four a) dimensions b) model displaying the metal washer. 37
Figure 3.12 - Sample five a) thickness and b) width of each area c) printed model. 38
Figure 4.1 - Nine groups of temperature values from the nine points of Sample One. 42
Figure 4.2 – Test 1 - evolution of temperature in each point. 42
Figure 4.3 – Results of Sample 1P Group one: a) outer defect 20s b) outer defect 30s c) middle defect 20s d) middle defect 30s e) inner defect 20s f) inner defect 30s. 43
Figure 4.4 – Test 9 – evolution of temperature in each point 44

Figure 4.5 - Results of Sample 1P Group two: a) outer defect 30s b) middle defect 30s c) inner defect 30s. 45
Figure 4.6 – Test 3 - evolution of temperature in each point. 47
Figure 4.7 - Results of Sample 1P Group three: a) outer defect 20s b) middle defect 20s c) inner defect 20s. 47
Figure 4.8 – Comparison between DATT and conventional APT a) Tests 2 and 8 b) Tests 3 and 8 c) Tests 4 and 8. 48
Figure 4.9 – Test 2 – evolution of temperature in each point. 50
Figure 4.10 – Results of Sample 1P Group four: a) test 1 b) test 2. 50
Figure 4.11 - Sample 1P Group four thermograms where all three defects appear at the same time a) 37 s after the beginning of the hot flow for test 1 b) 38 s after the beginning of the hot flow for test 2. 51
Figure 4.12 – Sample 1P Group three thermograms (reference test – hot only): a) instant of 21 s where the outer defect has the higher contrast b) instant of 36 s where the outer and middle defect can be seen c) instant of 50 s where the three defects can hardly be seen. 51
Figure 4.13 - Test 5 - evolution of temperature in each point. 52
Figure 4.14 - Results of Sample 1C: a) outer defect 20s b) outer defect 30s c) middle defect 20s d) middle defect 30s e) inner defect 20s f) inner defect 30s. 53
Figure 4.15 - Group one cold flow experiment a) areas measured b) temperature variations across the four areas. 55
Figure 4.16 - Temperature variation results a) test 1 b) test 2. 56
Figure 4.17 - Results of experiments with cooling fluid: a) temperature variation b) outer defect c) middle defect d) inner defect. 57
Figure 4.18 - Twelve groups of temperature values from the twelve points of Sample two. 59
Figure 4.19 – Test 1 - evolution of temperature in each point. 59
Figure 4.20 - Results of Sample 2: a) test 1 b) test 2. 60
Figure 5.1 - Reflection mode set-up a) variables α, d and d_p b) relation between α and d. 64
Figure 5.2 - Sample four experiments a) group one b) group two. 65
Figure 5.3 - Areas of sample four group one. 67
Figure 5.4 - Results of the experiment in which d=215.7 mm. 69
Figure 5.5 - Areas of sample four group two. 70
Figure 5.6 - Results of the experiment in which d=162.2 mm. 71
Figure 5.7 - Areas of sample three. 72
Figure 5.8 - Results of the experiment in which d=73.6 mm. 73
Figure 5.9 - Areas of sample three. 74
Figure 5.10 - Results of the experiment in which d=130.1 mm. 75

Figure A1 - Schematic representation of a) Rayleigh wave b) Lamb wave..... 84

LIST OF TABLES

Table 2.1 - Thermal properties of different plastics. 15
Table 2.2 – Sound wave properties of three mediums..... 22
Table 2.3 – Reflection and transmission coefficients of four boundaries. 23
Table 4.1 - First six experiments of Group one – 20 s. 41
Table 4.2 - Last six experiments of Group one – 30 s. 41
Table 4.3 - Experiments of Group three – 20 s..... 46
Table 4.4 - Experiments of Group four. 49
Table 4.5 - Experiments of Group two. 55
Table 4.6 - Experiments with cooling fluid. 56
Table 4.7 - Experiments of Sample two. 58
Table 5.1 – Range of possible values for each variable. 65
Table 5.2 - Experiments of Sample Four Group One. 66
Table 5.3 - Experiments of Sample four group two. 70

ABBREVIATIONS

3D	Three dimensional
ABS	Acrylonitrile Butadiene Styrene
ACU	Air-coupled Ultrasound
AM	Additive Manufacturing
DIC	Digital Image Correlation
FDM	Fused Deposition Modelling
FFF	Fused Filament Fabrication
IR	Infrared
IRT	Infrared Thermography
LIT	Lock-In Thermography
NDE	Non-Destructive Evaluation
NDT	Non-Destructive Testing
Ni-Ti	Nickel Titanium alloy
PA	Polyamide
PC	Polycarbonate
PEEK	Polyetheretherketone
PEI	Polyetherimide
PLA	Polylactic Acid
PMC	Polymer Matrix Composites
PT	Pulsed Thermography
PTFE	Polytetrafluoroethylene
UT	Ultrasound

SYMBOLS

α	Thermal diffusivity [mm^2/s]
ε	Emissivity []
λ	Wavelength [m]
ρ	Density [kg/m^3]
A	Sound amplitude [dB]
c_p	Specific heat [J/kgK]
e_t	Effusiveness []
f	Frequency [Hz]
k	Thermal conductivity [W/mK]
c	Velocity [m/s]
Z	Acoustic impedance [$kg/m^2/s$]

1 – INTRODUCTION

1.1 – Motivation

Recently, there has been an increased focus on the development of materials, like high-strength steels or composites produced by Additive Manufacturing (AM), in order to satisfy industrial and economic requirements, for example, in aerospace and automotive industries, where they seek reduced weight components, with enhanced strength, which improve productivity and fuel economy and reduce CO_2 emissions. This progress raises new demands in characterizing a variety of defects that may appear during its production and service life and which have an impact on the component's performance [1,2].

Examples of defects found in AM produced parts are delaminations between matrix layers [3], lack of bonding between the matrix and reinforcements [4], porosities, either as an inter-filament discontinuity or path discontinuity [5–7], support material which is trapped between internal surfaces [5], dimensional inaccuracy [8], thickness divergence [8], fibre and other reinforcements' misalignments [9], poor surface finish, such as the staircase defect [8,10], part warpage [8], and vibrations and ringing [11]. Among the consequences associated with these defects, there are the loss of mechanical properties, the afflicted performance of the produced components and its service time [5].

There are currently some challenges regarding the inspection of composites, mainly in polymer matrix composites, such as the complexity of the produced model [12], the inspection accessibility (for example, in pipe and tube manufacturing), the exposure to heat and other relevant properties of plastics, such as low thermal and electrical conductivity [13].

According to a review made by Gholizadeh [14], many NDT techniques are used to evaluate composites (contact and non-contact), like Ultrasonic testing (traditional and other variants, such as Air-coupled Ultrasound), Electromagnetic testing, Eddy Current testing, Magnetic Particle testing, Dye Penetrant Testing, Infrared Thermography testing, Radiographic testing, Visual Inspection and Shearography Testing, to name a few.

Visual Inspection (VI) is a cheap and rather fast technique but it is very limited to superficial defects. Magnetic particles has the limitation of only working with ferromagnetic materials and Dye Penetrant testing only allows access to one surface of the sample and the inspection of surface defects, does not give the depth sizing and it is a time-consuming technique, not to mention the environmental concerns of its usage [14].

As a laser optical method, Shearography testing has the great advantage of detecting the degree of strain concentrations around a defect and it is less susceptible to noise, compared to other NDT techniques. However, it is an expensive technique and the characterization of defects that are not delaminations is extremely difficult [14].

One of the most used technique is Ultrasonic testing (UT), which has the advantage of great scan speed, good resolution, flaw detecting capabilities as well as the possibility to be used in the field. Moreover, there is a variant, Air-coupled Ultrasound (ACU), which works in low frequencies, typically between 50 – 400 kHz, which doesn't require a contact coupling as the sound propagates through the air and can be used to inspect composites, since it avoids problems that arise from direct contact between the probe and sample. However, UT has a demanding assembly, requires skilled operators, especially to accurately interpret the results, and the defect size needs to be bigger than the wavelength to be detectable. Additionally, ACU represents a much slower inspection and doesn't allow the inspection of defects on the surface or very far from it [2].

Another NDT technique used is Eddy Current testing (EC), which is based on the electromagnetic induction phenomena produced by a current in a conductive material [15,16]. These current's strength relies in the electrical conductivity and magnetic permeability of the material, which are characteristics of electric conductor materials, so they are unfeasible for most composite materials with a polymeric matrix, although they

can be applied, in some extent, to inspect polymeric matrix with carbon fibres. However, unlike Infrared Thermography testing and Ultrasonic Testing, EC has proven to be a suitable technique for high-speed inspection of composites made of carbon fibres and reinforced plastic [17].

A NDT technique that can overcome some of the limitations presented so far is Infrared thermography testing (IRT), which acquires and processes the thermal response of an object, when excited by infrared radiation, and that uses an infrared camera and thermographic image software to acquire the surface temperature distribution of the object (thermograms) through time and space. Through the contrasts of temperature presented in these thermal images, it can be detected and identified superficial and internal defects in the object [18]. The main optically stimulated thermography techniques are active Lock-in Thermography (LIT) and active Pulsed Thermography (PT). LIT is an active IRT technique that detects and characterizes the internal damage based on the analysis of the thermal response of an object when stimulated by a thermal source with periodic modulation (stable state response). It requires few heat, as the thermal energy is concentrated in only one angular frequency, but is a rather slow technique, with expensive equipment, and the defects are only visible at a certain modulation frequency. PT is a technique where the detection and characterization of the internal damage are based on the analysis of the thermal response of an object when stimulated by a thermal pulse (transient response). It is a faster type of inspection and the thermal stimulation is shorter than the one from LIT but can only be used in composites that can be heated and may not be very effective at detecting internal defects at greater thickness.

One innovative technique that can overcome some of the problems mentioned is a variant of active IRT which uses two sources of heat, one of them being cold, which was addressed by Lei *et al* [19], and is a focal point of the present thesis.

Therefore, by continuing to research in order to understand and expand the techniques capability, we may increase awareness on how composite materials produced by AM may react in production and in-service phases and in turn, improve them for demanding jobs.

1.2 – Goals

The purpose of this work is to apply and test the reliability of different NDT techniques and its inspection parameters to evaluate composite material components produced by Fused Filament Fabrication. The work includes:

- The development and analysis of a new variant of the NDT technique Active Pulsed Thermography, *Double Active Transient Thermography* (DATT), to evaluate the temperature distribution and contrasts in the object surface and defect zone, through the application of heat and cold fluxes in different stages and different surfaces;
- The analysis of the NDT technique Air-coupled Ultrasound to evaluate the technique's resolution capability for different defects and different geometries in reflection mode.

1.3 – Thesis Structure

The present thesis is divided into six chapters and two appendixes:

- Chapter 2 presents an overview of the state of the art for the characterization of polymer matrix composites produced by AM using the two NDT techniques;
- Chapter 3 gives a brief description of the equipment necessary and set-up used in each NDT technique, and the five samples and their defects, produced by AM;
- Chapter 4 presents and discusses the results achieved with the Double Active Transient Thermography experiments;
- Chapter 5 presents and discusses the results achieved with the Air-coupled Ultrasound experiments;
- Chapter 6 summarizes the main conclusions of the work presented and outlines topics and recommendations for future research;

2 – LITERATURE REVIEW

2.1 – Introduction

This chapter reflects the bibliographical review made with the goal of characterizing the two NDT techniques used to evaluate composites and polymer matrix composites produced by AM.

Composites have existed for a long time, since Ancient Mesopotamia and Egypt Civilization, with different types being developed for several applications. In the beginning of the 20th century, plastics like vinyl and polystyrene were developed, and Bakelite was created, marking the first step towards the modern era of composites, and around 1935, it was introduced the first glass fibre. Thenceforth, new materials were developed, with great advancements being made during World War II, until nowadays, with developments in industries like aerospace and renewable energy [20].

In turn, AM technology has been around for almost four decades, emerging in 1981, with the first 3D printing patent being awarded to Dr. Hideo Kodama, in Japan, who developed a photopolymer rapid prototyping technique, using UV light, to build up a solid, printed model in layers. Since then, many more processes, materials, products, tools and

businesses were developed and perfected. AM has become more and more industrialized, with applications in fields such as medical industry, aerospace industry, transportation industry and consumer products industry [21].

Non-Destructive Testing (NDT) have existed for many centuries, starting with Visual Inspection (VI), which was used to inspect components like clay pots and to inspect metal surfaces with chalk, for instance. One NDT technology, the Ultrasound technique (UT), started being studied for the purpose of detecting flaws in metal objects by soviet scientist Sergei Y. Sokolov, around the 1930's, inspired by the sonar technique. During World War II, pulsed ultrasonic testing using a pulse-echo technique was developed and patented and in the decades that followed, UT was refined and became a trusted resource by manufacturers for flaw detection as well as an imaging technique for medical diagnostic. The UT equipment and techniques have evolved significantly, with digital instruments being developed to provide stable calibration, precise measurements, data retention, and screenshot sharing capabilities [22].

Regarding Infrared Thermography Testing (IRT), another NDT technology, most techniques were patented also in the Second World War, with applications in fields such as machinery and communications, and later developed to analyse temperature distribution in automobile brakes and overheating of electronic components, among others. Infrared radiation was firstly discovered in the beginning of the 19th century, by Sir W. Herschel, when he was conducting Sir Isaac Newton's experiment decomposing white light into a range of colours. From then on, many inventions appeared, for example, the thermocouple, in 1829, and the first infrared image, in 1840, by means of a evaporograph [23]. Infrared-based tools are used for the inspection of components and structures in fields like wind power, automotive and aerospace industries, for example, to detect layer structures, delaminations and inserts in wind turbines blades and carbon fibre reinforced plastics (CFRPs) [18].

2.2 – Polymer Matrix Composites

A composite material is a material formed by two or more elements, usually different types of materials, which has properties that are different from those of the individual elements. One of the elements is the matrix material, a continuous phase, which can be metal, inorganic non-metallic or polymer, according to Wang *et al.* [24]. The other

element is the reinforcement material or auxiliary material, a dispersed phase, which can be of various types, such as particles, flakes and fibres [24].

Polymer Matrix Composite (PMC) is an example of composite material, in which the matrix is made of polymer and the reinforcement material, usually a fibre, is added to the matrix, as shown in Figure 2.1, to improve the properties of polymers for higher-strength demand applications, making it a stronger and less ductile material [25].

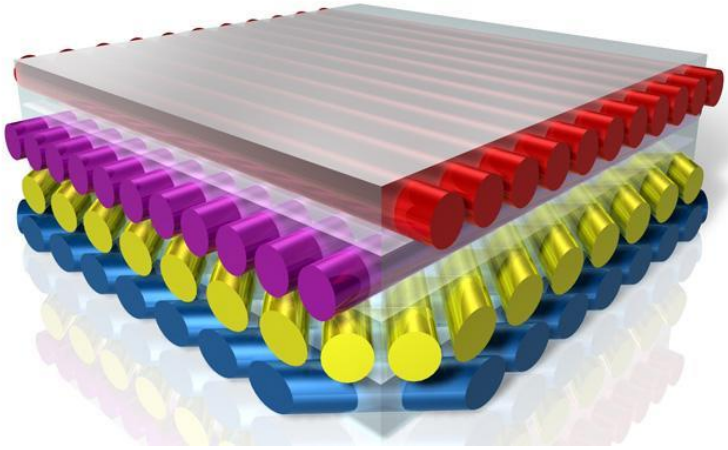

Figure 2.1 - Example of the structure of a fibre-reinforced composite [24].

Some advantages of PMC are the ease of fabrication, compared to the other types of matrices; the ease of connection between polymers and fibres, the enhanced properties that result from the bonding and the low density of polymers [26].

2.2.1– Polymer Matrix

Usually, additives are added to the resin matrix to improve or add properties that the polymer may not have, such as enhancing the stability of the polymer, as a prevention to the aging and degeneration of the material, enhancing the mechanical properties, improving processing performance, reducing the melting temperature and increasing the mobility and flexibility of the materials [24].

The most common matrix materials used are thermoplastics, which soften and melt when heated, such as Fluoropolymers, Polyamides, Polyesters, Styrenics, Polyimides, and Polyethers; and thermosets.

In Appendix 1, it is given a brief description of some matrix materials, namely, Polytetrafluoroethylene (PTFE), Polyamide (PA), Polylactic Acid (PLA), Acrylonitrile Butadiene Styrene (ABS), Polyetherimide (PEI), Polyetheretherketone (PEEK), Polycarbonate (PC) and Epoxy [27].

2.2.2– Reinforcement Material

This material improves significantly the mechanical properties of the polymer matrix. The most effective are the fibrous materials, such as carbon fibres, glass fibres, alumina fibres, silicon carbide fibres and organic fibres, because their strength and elastic modulus is much higher than of the matrix material.

Some examples of reinforcement materials used are:

- **Nickel Titanium alloy, Ni-Ti**, which is composed of titanium (Ti) and nickel (Ni), in the same amount, and that are used in biomedical applications and structure engineering, for example, due to its properties, shape memory effect (free recovery) and super elasticity;
- **Aromatic polyamide fibres (aramid)**, for example, Kevlar® (developed and traded by Dupont USA), which is an organic fibre used in demanding applications, such as ropes and cables, bulletproof vests, tennis strings, and snowboards, because of its toughness, thermal stability and corrosion endurance, among other features;
- **Glass Fibre**, an inorganic non-metallic material, in which silicon dioxide (SiO_2) is the main component of glass, used in fields like transportation and aerospace, among others, and with good performance, for example, noninflammability, resistance to heat-and toughness;
- **Carbon Fibre**, which is mostly composed of carbon atoms and with potential benefits due to its high stiffness and tensile strength, low weight, corrosion resistance and good conductivity. It is very used in fields like civil engineering and aerospace.

2.2.3– Defects in PMC

There are many defects that occur during production and/or during the material's operating life. Defects in fibres, such as fibre breakage, wrinkling and misalignment, induced in the production of the PMC material, may weaken them, and introduce stress concentrations in the material, therefore, reducing the mechanical properties.

In production and storage phases, problems in the matrix can arise due to contamination that leads to poor cure, because of incorrect storage, temperature and humidity. Porosity is also a concern, that can coalesce and become a void, with the outcome of introducing internal stress concentrations, and/or create delaminations in the material [28].

In-service, when the materials are subjected to cycles and loads, defects like matrix cracking and separation between fibre and matrix, which can lead to water infiltration and therefore, reduction in modulus; delamination, that can reduce the compressive strength and increase the chance of buckling, and fibre breakage, which reduces the tensile performance. Figure 2.2 represents some of the defects mentioned above [29].

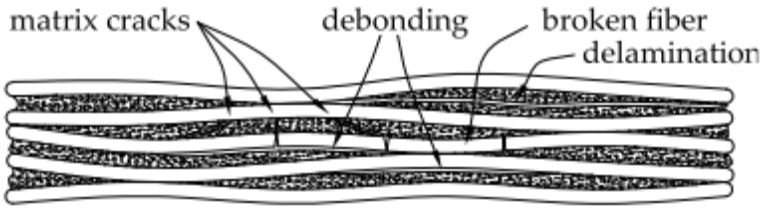

a)

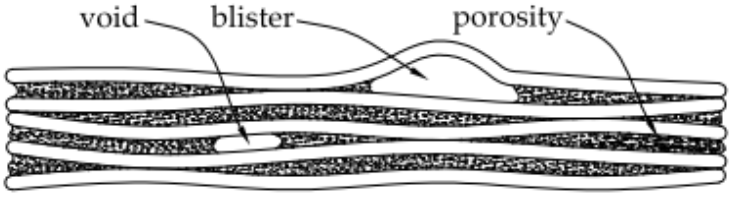

b)

Figure 2.2 - Examples of defects in PMC [29].

2.3 – Additive Manufacturing

Additive Manufacturing (AM), also referred to as 3D printing, is the technology that manufactures an object by depositing layers of material [30].

According to the American Society for Testing and Materials (ASTM) group "ASTM F42 – Additive Manufacturing", there are 7 categories of AM: VAT Photopolymerization, Material Jetting, Binder Jetting, Material Extrusion, Powder Bed Fusion, Sheet Lamination and Directed Energy Deposition [31].

2.3.1– Fused Filament Fabrication

Fused Filament Fabrication (FFF) is a material extrusion process commonly used for 3D printing which uses a thermoplastic material. Although the terminology Fused Deposition Modelling (FDM®) is most used, it is trademarked by the company Stratasys [32].

As shown in Figure 2.3, in this technology, the material, in the form of a filament, is loaded into a heating chamber, where it liquefies forming a high-viscosity material and then moves as a continuous stream through the extrusion nozzle.

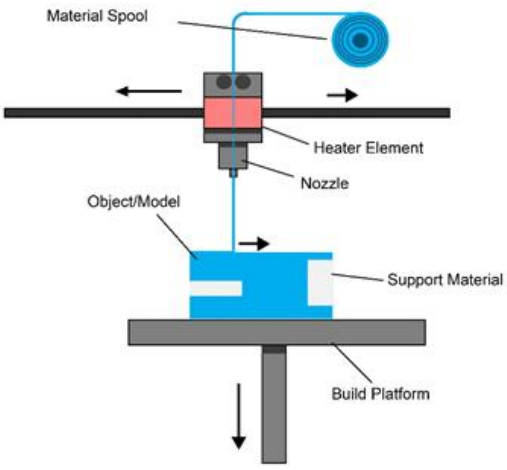

Figure 2.3 - Schematic representation of a typical FFF setup [33].

The first layer of the material is extruded into the print bed, followed by other layers that are added on top of previous ones. The material is bonded to itself or another

secondary material, usually by means of temperature control, to form a solid structure. There is usually the inclusion of support structures for supporting complex figures, during the fabrication process [34].

2.3.1.1 – Materials used in FFF

The current commercial materials directly processed by this material extrusion process are ABS, PLA, PA, PC, PEI and PEEK, according to Bourell *et al*. [35]. Material extrusion processes use thermoplastic polymers, most commonly amorphous thermoplastics, because they melt in a variety of temperatures, becoming ideally viscous for material extrusion through a 0.2–0.5 mm diameter nozzle [35].

Regarding PMC, according to the same authors, there are already commercial machines capable of printing composite filaments, for example, embedding continuous carbon fibre, chopped carbon fibre, Kevlar, and fiberglass in a nylon matrix [35].

2.3.1.2 – Parameters of FFF

The process parameters of FFF commonly considered are [36]:

- **The layer thickness**, the height of the deposited layer made by the FFF nozzle;
- **The orientation** of the part, defined as how the part should be positioned when produced;
- **The raster angle**, the orientation of material deposition on the XY-plane;
- **The raster width**, the thickness of material deposition on the XY-plane;
- **The material feed rate**, the requested speed for the 4 axis, X, Y, Z and E. X, Y and Z are used for moving the printhead in space and E is used for the amount of filament to be moved into the printing head;
- **The printing temperature**, the temperature at which the filament turns into a viscous substance that can be extruded;
- **The print bed temperature**, the temperature of the surface where the extruded material will adhere, and the structure will be built layer-by-layer.

Figure 2.4 presents some of the parameters mentioned.

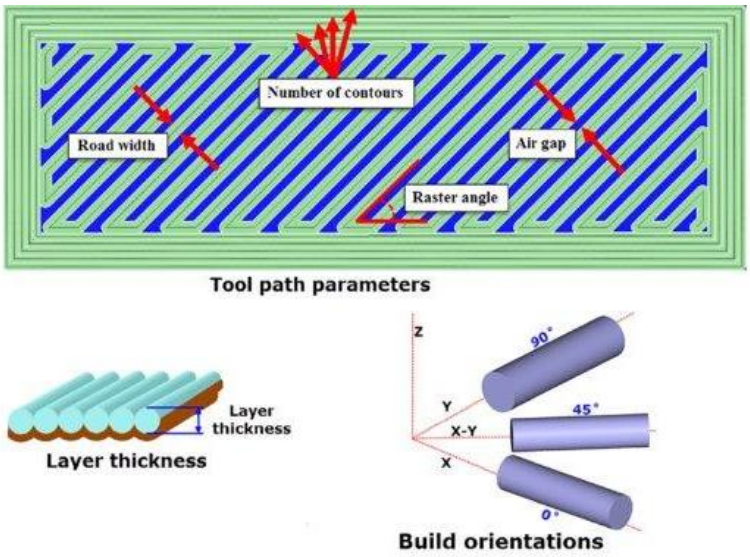

Figure 2.4 - Examples of FFF parameters [37].

2.3.1.3 – Defects and disadvantages of FFF

The most common defects found in the FFF process are voids, anisotropy, poor surface quality, distortion and warping, dimensional and geometric deviations. Three of these defects are shown in Figure 2.5.

- **Voids** are areas with lack of material, usually between the deposited tracks of extruded material, though they're rare and very dependent on the material (for example, Nylon) (Figure 2.5 a));
- **Anisotropy** is a feature of materials in which their physical and mechanical properties vary along different directions;
- **Poor surface finish/quality** vary from material and appears on finish pieces. One example is the staircase effect shown in Figure 2.5 b);
- **Distortion and warping** of the pieces happen due to expansion and contraction of the plastics, as they are printed, which causes the print to bend up from the build plate (Figure 2.5 c));
- **Dimensional and geometric deviations** are defects that can be crucial for functional parts [35,38].

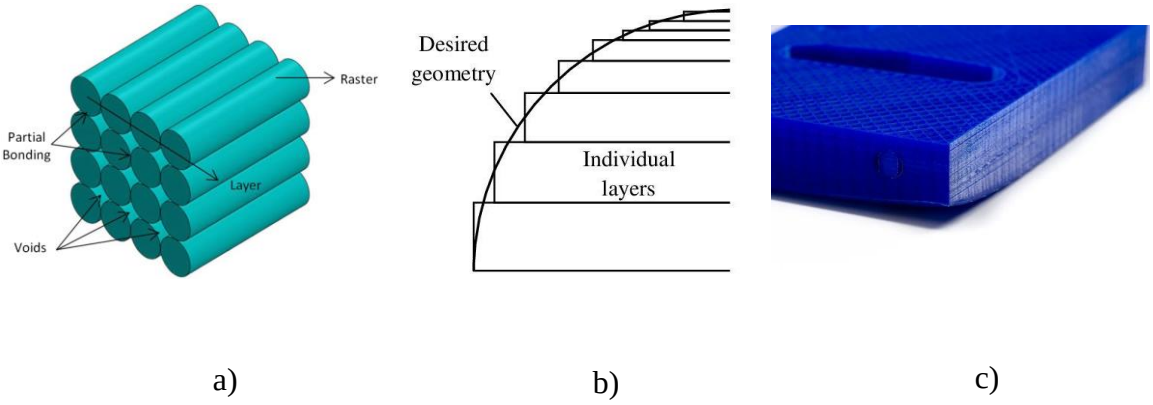

a) b) c)

Figure 2.5 - Example of defects found in FFF: a) voids [39] b) 'staircase' effect [40] c) warping [41].

Apart from the common defects presented, printing materials with FFF technology are limited by the nozzle radius and clogging, which can compromise the quality of the final model, the accuracy and speed, and the quality of the printed material is still low, comparing to other processes to manufacture composite materials, like automated tape laying and out-of-autoclave process, to improve the final part quality [35,38].

2.3.2- State-of-the-art of composites produced by AM

Recent papers have been published regarding the advancements made to produce composites through AM, especially to meet the new requirements of the aerospace industry.

In their latest paper, Díaz-García *et al.* [42], present a laboratory scale methodology to extrude magnetic composite filaments using FFF, and which X-Ray Tomography results show to produce soft and consistent continuous filaments with great dimensional control, suitable for different polymer matrices and other particle types, rather than magnetic ones.

A recent paper written by Chang *et al.* [43], refers that continuous carbon fibre reinforced poly-ether-ether-ketone composites, produced by the Laser-assisted Laminated Object Manufacturing technique and hot press postprocessing, exhibit superior mechanical than carbon fibre reinforced thermoplastics produced by FFF.

Additionally, Kim *et al.* [44], assess some formulations to print polyetherimide nanocomposites, with enhanced thermal properties, using FFF machines, in order to

produce thermal protection systems using AM. The results show that four of the eleven formulations present composites with enhanced features.

One review of the state-of-the-art of fibre-reinforced polymers was made by Blok, *et al.*[45], in which they characterise and compare the mechanical properties of parts produced by short fibre printing method and continuous fibre printing method, in which the latter provides better properties. They conclude that the quality of parts produced by FFF are still of low quality, with common formation of voids and limited control when placing a fibre, when compared to classical aerospace composites; that reinforced filament show great improvement in mechanical properties, when compared to unreinforced ones, but they still need to be higher if to be used in structural materials; and that there is lack of coherent information available regarding how different printing parameters affect the quality of the final product and detailed information of defects that may occur.

Another review was made by Brenken *et al.* [46], where they summarise the reporting of mechanical properties both for short and continuous fibres. As with the previous authors, they also mention the void formation, as well as fibre damage, that occur during the printing process and which prevent discontinuous fibre-reinforced polymers to be on the level of aircraft aluminium, but that continuous fibres show strengths close to the aluminium ones, although proper wetting of the fibres needs to be made during printing as well as increasing the fibre volume fraction. They outline some advantages of AM, such as time and cost savings, but refer that, to date, few relevant works in the area have been published.

2.4 – Active Pulsed Thermography

Infrared thermography testing (IRT) is a NDT technique that acquires and processes the thermal response of an object, excited by infrared radiation, and that uses an infrared camera and thermographic image software to produce thermograms (thermal images) where there can be detected and identified internal defects through the contrasts of temperature presented [18].

2.4.1 – Properties and types of techniques

The most important thermophysical properties when inspecting an object using IRT are thermal diffusivity, thermal conductivity, density, specific heat capacity, effusiveness and emissivity.

- **Thermal conductivity**, k [W/mK], measures the ability of a material to conduct heat;
- **Density**, ρ [kg/m^3], is a measure of mass per volume unit;
- **Specific heat**, c_p [J/kgK], at constant pressure, is the amount of heat necessary in one unit of mass of a substance in order to increase one unit of its temperature;
- **Thermal diffusivity**, α [mm^2/s], measures the ability of heat transfer of a material when compared with its ability to store that heat. It is inversely proportional to ρ and c_p and directly proportional to k;
- **Effusiveness**, e_t, is a measure of the capability of a material to exchange heat with its surrounding;
- **Emissivity**, ε, is the capability of a material to emit thermal radiation.

Table 2.1 shows the thermal properties of some plastics.

Table 2.1 - Thermal properties of different plastics [47].

Material	Specific Heat [J/kgK]	Thermal Conductivity [W/mK]	Thermal Diffusivity [mm^{2}s^{-1}]
ABS	1468	0.18	0.12
PC	1300	0.23	0.15
PA	1700	0.26	0.13
PEEK	1340	0.25	0.14

Regarding the thermography techniques, there are two basic types:

- **Passive thermography**, where there is a difference between the natural temperature of the object and the defect, which must be sufficiently high to be detected by the IR sensor. One limitation is that, when the difference of

temperature between the object and defect is zero, the technique cannot detect the flaws;

- **Active thermography**, where there's an external thermal stimulation of the object to create a heat flux within the material, which generates a difference in temperature between the object and defect and allows the detection and characterization of defects.

The main optically stimulated thermography techniques are active Lock-in Thermography and active Pulsed Thermography or Transient Thermography. There are other secondary techniques that are special cases of the two main ones and that differ in the thermal stimulation of the object and the thermographic data analysis.

Lock-In Thermography (LIT) is an active IRT technique that detects and characterizes the internal damage based on the analysis of the thermal response of an object when stimulated by a thermal source with periodic modulation (stable state response). This technique uses a continuous heat source that generates a thermal wave that propagates to the interior of the inspected object and reveals the presence of defects after reaching a stable state. This technique requires lower heat, as the thermal energy is concentrated in only one angular frequency and the determination of the depth of the defect is made almost direct since it's inversely proportional to the angular frequency.

Pulsed Thermography (PT) is a technique where the detection and characterization of the internal damage is based on the analysis of the thermal response of an object when stimulated by a thermal pulse (transient response). It is a faster type of inspection and the thermal stimulation is shorter than the one from LIT. The surface of the object can be heated by a thermal pulse and then measure its temperature decay, or it can be applied a cold pulse and measure the increase in its temperature. Figure 2.6 shows a schematic view of a PT system configuration consisting of lamps, specimen, camera and processing computer [48].

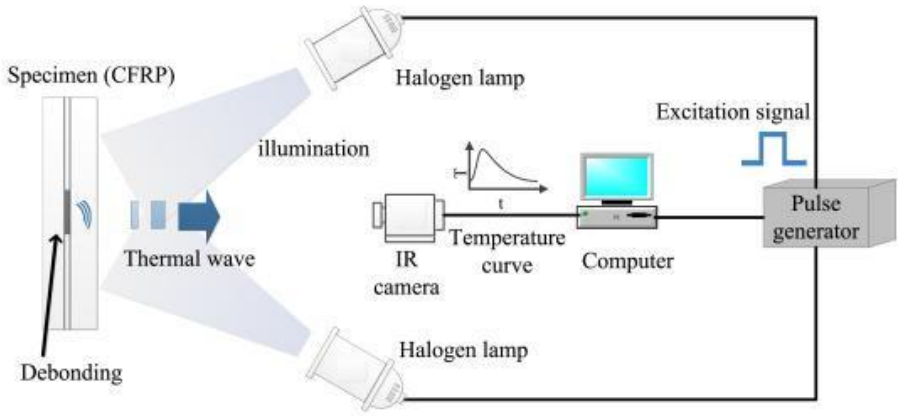

Figure 2.6 - Schematic view of a pulsed thermography inspection [48].

The heat sources produce thermal pulses that can last seconds depending on the thickness and material of the object. Examples of this sources are incandescent light bulbs and heat radiators. The IR cameras are designed to operate in specific infrared spectrum bands. Fluke Ti400, the camera used in the present work, has a spectral range of 7.5 to 14 μm [49].

There are two configurations when inspecting an object using PT: reflection mode and transmission mode, as shown in Figure 2.7 [50].

- **In reflection mode**, the IR camera and the heat sources are placed in the same side. The advantage of this configuration is that only one side of the object needs to be visible, but it's limited to the detection of superficial defects;
- **In transmission mode**, the IR camera and the heat sources are placed in different sides. It can detect subsurface defects although there's loss of thickness depth notion and requires access to both surfaces. This configuration represents a great limitation when it isn't possible to access both surfaces, for example, when inspecting pipes.

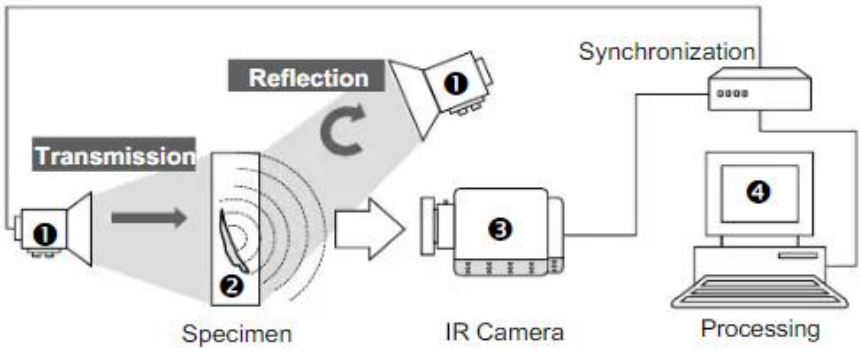

Figure 2.7 - Reflection and transmission modes [50].

2.4.2 – Thermography data

As mentioned before, IR cameras allow the acquisition of thermograms that show the temperature distribution in a specific object. The next pair of images show two examples where IRT can be used, namely in the plastics industry (Figure 2.8 a)) and aerospace industry (Figure 2.8 b)).

a) b)

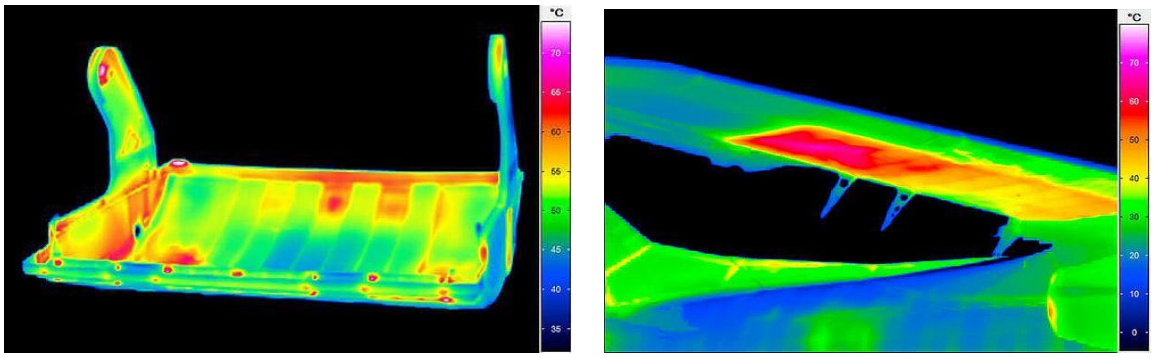

Figure 2.8 - Examples of IRT applications a) temperature distribution of plastics in injection moulds [51] b) temperature distribution of composite materials [52].

2.4.3 – Limitations of IRT

Although this type of inspection is a fast one, easy and safe to use, with many possible applications, there can be losses of heat, mainly through atmospheric absorption, it's difficult to obtain an uniform heating, even more when using curvilinear objects, and for greater material thickness, the inspection may take more time and the defect may not be

visible through the camera, mostly with transmission mode, as the heat travels through the sample thickness [1].

Additionally, passive thermography only works with enough natural thermal contrast between the object and defect. LIT takes longer to inspect, when compared to PT and the defects are only visible at a certain modulation frequency. PT has the limitation of requiring, sometimes, the prior knowledge of the defect free zones [23].

2.4.4 - State-of-the-art of PT for Polymer Matrix Composites evaluation

Unlike Air-Coupled Ultrasound (ACU), infrared thermography has more research published, especially to test aerospace components. Not all articles are mentioned in this dissertation, as it was given priority to the most recent ones that address the use of this technique in PMC or composites in general to determine its detection limit and resolution and also the ones where the material is produced by AM.

In an experiment, published by Machado *et al.* [2], four different samples were evaluated, a flat PLA matrix sample with voids of 0.5 mm thickness to simulate delaminations, a similar sample but with a curved shape, a PLA matrix with three 0.1 mm thickness PTFE tapes and a PLA sample with two 0.25 mm NiTi wires imbedded. The fourth sample was evaluated using passive IRT, which clearly showed the contrast between defect and free zone. The other samples were evaluated using PT, both with reflection and transmission mode, where the defects were clearly visible with good resolution. With reflection mode, there were a clearer contrast, but the heat distribution was more heterogenic. For transmission mode, there was a more uniform heat distribution, but the void resolution was poorer and there was the need to access both sides of the object. With the curved sample, comparing with the flat one, in reflection mode there was a bigger lack of heat uniformity, which lowered the delaminations detection capability, but in transmission mode, the difference was insignificant.

In an article published by Cramer [53], of NASA Langley Research Center, it is mentioned the use of active PT for rapid, large-area inspection of complex composite structures used for aeronautics and space vehicles. They show an example of qualification of manufactured parts using IRT, a CFRP component of the Space Shuttle where it is visible dark regions, areas of excess resin, and light regions, areas of poor material

bonding They also use IRT for on-orbit inspection of manned vehicles and the International Space Station (ISS) using the solar heating as thermal source.

In an article published by Dattoma *et al.* [54], two T-shaped stringers and three laminated flat plates, made up of CFRP, were investigated through reflection mode, to identify the optimal configuration for defect detection. For the T-shape stringers, there were various set-up configurations with different distances between lamps, lamps and the object and between the camera and the object. For the laminated flat plates, there were used four halogen cameras and the distance between lamps and object were 100 cm; the experiments were performed with different heating and acquisition times and different distance between camera and object.

Lei *et al.* [19], conducted an experiment regarding three different stimulation techniques, PT (as reference), LIT and Liquid Nitrogen cooling, which was poured directly onto the surface of the sample, a steel specimen with flat-bottom voids with different depths and sizes, in reflection mode. The researchers concluded that all three techniques show parts of the defects, with the most detectable being those with higher diameter to depth ratio, and that with Liquid Nitrogen cooling, the defects only appeared at the beginning of the cooling process, probably due to the high conductivity of steel. In future researches, they propose analysing different types of specimens, changing the method of pouring the Liquid Nitrogen and to test the application of heat on one side of the object and cooling on the other side.

Additionally, Pastuszak [55] investigated the ability of PT to detect defects in Glass Fibre Reinforced Plastics (GFRP) cylindrical panels and proved the effectiveness of the technique to test curved composite structures and that it can be successfully simulated through numerical simulation.

2.5 – Air-Coupled Ultrasound

Ultrasonic testing (UT) characterizes the physical condition of an object through the use of high-frequency sound waves. The frequencies used for UT are higher than the limit of human hearing, usually between 0.5 and 25 MHz [56].

Ultrasonic technology is used in critical safety-related and quality-related applications, in industries like aerospace, marine and automobile, more specifically, in

manufacturing, weld inspection, infrastructures and in-service testing, and also in the biomedical field for diagnostic imaging and medical research.

2.5.1 – Physics of Ultrasound

Ultrasonic waves, or mechanical vibrations, are originated by the alternate compression and rarefaction zones produced by the vibration of the elementary particles that constitute the material. They can propagate through solid, liquid and gas mediums but not through a vacuum. The waves are described by a sinusoidal wave equation with amplitude A [dB], frequency f [Hz], wavelength λ [m] and velocity c [m/s]. The velocity of sound waves is fixed in a specific medium and the wavelength is of great importance when identifying a discontinuity [57].

In ultrasonic inspection, the technique's ability to locate discontinuities is usually described by its sensitivity, which is the capacity of locating small discontinuities, and by its resolution, which is the capacity of the system to locate discontinuities that are close together with the material or near its surface. Both these terms increase with higher frequency, or shorter wavelengths. The ability to detect discontinuities by ultrasound are also affected by many other variables [57].

There are other features of sound wave important for UT, such as its attenuation, acoustic impedance, reflection and transmission coefficients, Snell's law and critical angles:

- **Attenuation** is the reduction of the sound intensity / pressure, due to factors such as the sound reflecting in other secondary directions and its energy being converted into other forms of energy. The acoustic attenuation varies with the material and frequency;
- **Acoustic impedance**, Z [$kg.m^{-2}.s^{-1}$], reflects the resistance met by an ultrasound beam, when it goes through a medium, and depends on the density of the medium, ρ [kg/m^3], and the speed of the sound wave, c [m/s], as shown in Equation 1;

$$Z = \rho c \qquad 1$$

- **Reflection coefficient**, R, indicates how much of the sound wave is reflected when it passes through the boundary between mediums 1 and 2 and it's dependent on the acoustic impedance of each medium, as shown in Equation 2 (in terms of sound pressure);

$$R = \frac{Z_2 - Z_1}{Z_2 + Z_1} \quad (2)$$

- **Transmission coefficient**, T, indicates how much of the sound wave is transmitted when it passes through the boundary between mediums 1 and 2 and it's dependent on the acoustic impedance of each medium, as shown in Equation 3 (in terms of sound pressure);

$$T = \frac{2Z_2}{Z_2 + Z_1} \quad (3)$$

- **Snell's Law** describes the relationship between the angles and velocities of the waves. Through this formula, the first critical angle can be calculated;
- **Critical angle** is the angle of incidence in which the refracted wave has a refraction angle of 90º. Above this critical value, the refracted wave will suffer an internal reflection.

Table 2.3 presents the reflection and transmission coefficients of four types of boundaries, Air / PLA, PLA / Air, Air / ABS and ABS / Air, based on the values of Table 2.2 (air values at room temperature), which reflects the difficulty to transmit a sound beam across Air – PLA – Air and Air – ABS – Air. The reflection coefficient values are high because of the great difference of acoustic impedance between the air and the PLA.

Table 2.2 – Sound wave properties of three mediums [58,59].

Medium	ρ [kg/m^3]	c [m/s]	Z [kg.m^{-2}.s^{-1}]
ABS	1050	2250	2362500
PLA	1240	2220	2752800
Air	1.2	343	411.6

Table 2.3 – Reflection and transmission coefficients of four boundaries.

Boundary	R	T
Air / PLA	0.99970	1.9997
PLA / Air	- 0.99970	0.0003
Air / ABS	0.99965	1.99965
ABS / Air	- 0.99965	0.00035

Regarding the sound waves propagation, the basic types are longitudinal waves (the most important waves for Air-coupled Ultrasound), where the trajectory of the waves is parallel to the direction of its oscillation and can propagate through solids, liquids and gases; and transverse waves, where the trajectory of the waves is at right angles with the direction of its oscillation and can propagate only through solids. The velocity of the sound wave can be calculated through Equation 4, given the medium's frequency, f [Hz], and wavelength, λ [m].

$$c = f\lambda \quad (4)$$

In the air, the sound travels in the direction of the wave, although in solids, there can occur vibrations in other directions, so there are many more possible modes of wave propagation, useful for UT. Two of these modes are briefly presented in Appendix 2.

When the waves encounter a boundary with another medium with different acoustic properties (like air) or a discontinuity, there are different scenarios that may occur [57]:

- Some of the sound waves are reflected to the source and some are transmitted to the other medium, stablishing a relationship between reflected and transmitted sound dependent on the acoustic impedance;
- The beam falls obliquely into the surface, where some of the sound waves are reflected to the source and some are refracted, because of Snell's Law. In this case, reflected sound encounters variation in angle and intensity and in case the beam reaches the surface with critical angle, as mentioned before, the angle of refraction will be 90º (Figure 2.9 a));
- In case the wave encounters a small discontinuity or an opening, smaller than the wavelength of the wave, it will diffract (Figure 2.9 b)).

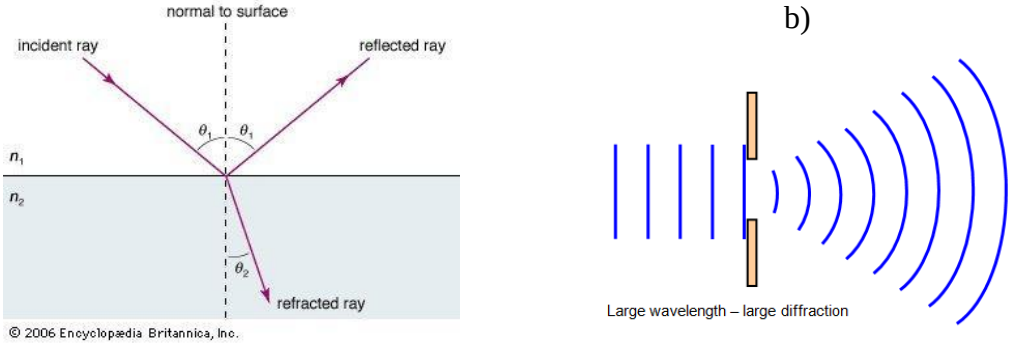

Figure 2.9 - Schematic representation of a) refraction [60] b) diffraction [61].

For the sound to be reflected and, therefore, the defect detected, the wavelength of the ultrasound must be smaller than the dimension of the defect. Otherwise, instead of reflection there will be diffraction. By analysing this behaviour and by knowing the travel time, the speed of propagation of the sound in the medium being inspected and the angle of emission, it is possible to find evidence of discontinuities.

2.5.2 – Equipment and transducers

In a general way, the UT equipment is composed of a transducer, pulser/receiver and a display device, as shown in Figure 2.10. The pulser/receiver is an electronic device that can produce high voltage electrical pulses. An ultrasonic transducer converts electrical energy into mechanical vibrations that propagate through the materials and again into electrical energy upon the reflected wave, which is then shown on the display device. During the inspection, the transducer is typically separated from the object by an ultrasonic couplant, which facilitates the transmission of sound between the transducer and the object, to avoid attenuation effects (because of the air) and acoustic impedance [62].

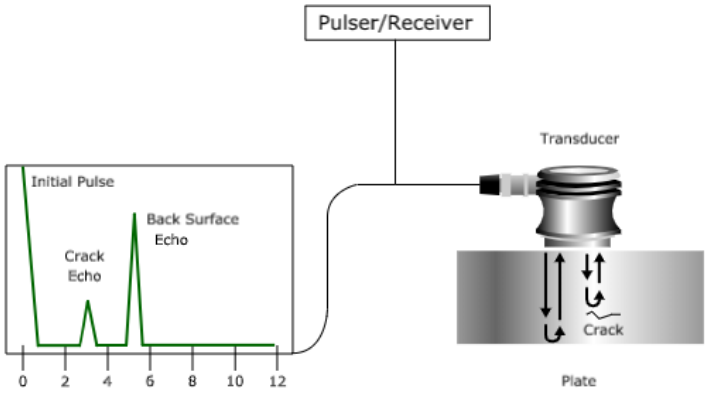

Figure 2.10 - Ultrasound system [62].

There exist various types of ultrasonic transducers, such as contact transducers, immersion transducers, angle beam transducers, delay line transducers and dual element transducers. Dual element transducers are composed of two elements, a transmitter and a receiver, which are assembled on a delay line at a small angle to create a crossbeam sound path in the test material. They are commonly used for thickness measurements of thin materials, high-temperature testing, since most duals will tolerate contact with hot surfaces, and for flaw detection in rough-surfaced castings [57].

2.5.3 – Air-Coupled Ultrasound

Air-coupled Ultrasound (ACU) has different equipment than the conventional Ultrasound because it's a non-contact technique and uses the surrounding air as couplant. Air-Coupled transducers are dual element transducers that work as transmitter and receiver. They usually operate at frequencies between 50 and 400 kHz and can be used for evaluating materials such as foams, plastics and composites. The most used methods of testing are transmission, shear waves and plate waves, as shown in Figure 2.11. Air-Coupled Ultrasound (ACU) has the great advantage of using the surrounding air as the ultrasonic couplant, identifying defects such as voids, cracks and disbonds in a wide variety of water-incompatible materials [63].

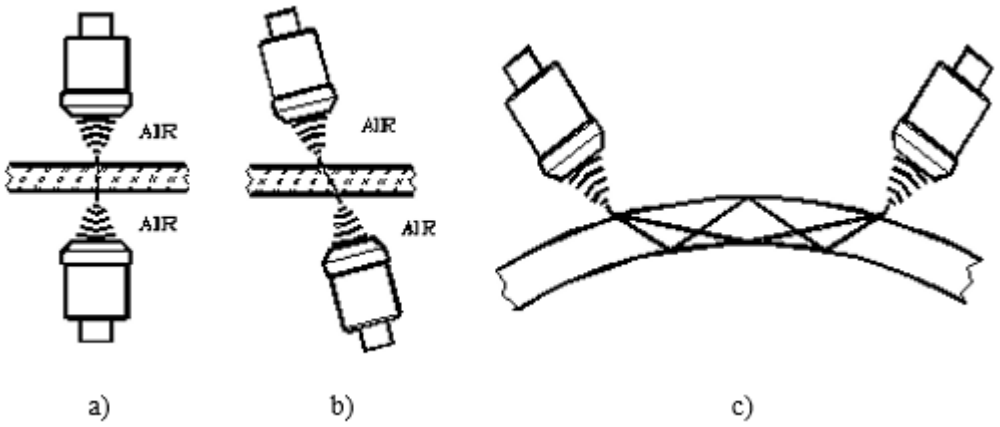

Figure 2.11 - Methods of testing a) transmission b) shear wave c) plate waves [63].

2.5.4 – Data presentation

The data from the inspection can be presented in different formats that provide different ways of evaluating the region inspected.

- **A-scan** plots the amount of received ultrasonic energy as a function of time;
- **B-scan** provides a two-dimensional graphic presentation (linear scanning) that plots the linear position of the transducer as a function of time, providing information about the size and the depth of a defect;
- **C-scan** presents a two-dimensional presentation (XY scanning), in which the location and size of discontinuities identified through the scanning are displayed in a top view of the material surface under test, allowing for an integrity diagnosis.

2.5.5 – Limitations of UT

Although Ultrasound Testing has high penetration capacity, good resolution, access to instantaneous results, high sensitivity to subsurface and in volume discontinuities, among other advantages, it is very sensitive to coupling, detection may require experienced operators and it's inadequate for complex geometries and materials with high acoustic attenuation coefficients, such as cast iron.

Although ACU may prevent the disadvantages of coupling water, like corrosion and air-bubbles in the coupling path, and allows fast two-dimensional scanning (C-Scan), it is still difficult to transmit sound waves through air and the technique is not suitable for complex geometries.

2.5.6 - State-of-the-art of ACU for Polymer Matrix Composites evaluation

There have been published many articles regarding ACU, mainly about its transducers, but there aren't many articles about its evaluation of PMC. Some recent experiments to determine the detection limit and resolution of this technique for the evaluation of PMC are mentioned below.

In the same article mentioned before and published by Machado *et al.* [2], the four samples were also evaluated through ACU, using a 200 kHz probe with a 11 mm diameter piezoelectric. For the evaluation of the first two samples, there was a clear output of delaminations. For the evaluation of the third sample, the tapes were visible but with poorer resolution and it was not perceptible in which plane the delaminations were present. For the fourth sample, the wires were too thin to be detected.

Other experiments were conducted regarding materials with reinforcement fibres and thermoplastic matrices. For example, Joas *et al.* [64], conducted an experiment with CFRP pipes and Essiga *et al.* [65], conducted an experiment with carbon fibre and polyamide 6. Neuenschwander *et al.* [66], performed three experiments regarding surface topography, transmission inspection and integrity checking of polymer and polymer-matrix composite samples, namely craquelure, plexiglass lens and silicon polymer (containing a fingerprint). Some conclusions of the experiments are the capability of ACU to obtain detailed imaging of surface topographies and high contrast imaging, measure the sound velocities and thickness variations and localize and measure delaminations. The researchers also concluded that some cracking may interfere with the attenuation by giving locally higher transmission amplitude spots [66].

2.6 – Chapter resume and conclusions remarks

This chapter gives a global overview of composites and Polymer Matrix Composites, Additive Manufacturing, more precisely, Fused Filament Fabrication, and two different

NDT techniques, including what has been researched as to the capability of the techniques to evaluate composites.

From the literature review, Infrared Thermography is more used to characterize defects in composite materials, especially in the aerospace industry, compared to Air-Coupled Ultrasound, although there are not so many articles published where these two techniques are used to characterize polymer matrix composites produced by AM. Plus, and as referred by the authors of some articles, there are still areas that can be deeper studied, for example, in Thermography, with the application of cold flux on one side of the specimen and heat on the other side and the application of the cooling process in curved samples as well as experimenting this variation in other materials, such as PLA, rather than only on CFRP and GFRP.

3 – EXPERIMENTAL PROCEDURE

3.1 – Introduction

This chapter describes, in detail, the specifications of the equipment for each technique and the set-up of each type of experiment, as well as the five samples and its artificial defects, which were produced by FFF. All samples were produced with an infill of 100%, in order to clearly distinguish the defects' area from the free-defect area during the inspections. Samples One and Two were printed in the vertical position, as shown in Figure 3.4 b) and Figure 3.8 b), in order to avoid the collapse of the printed layers over the voids, which simulate the defects.

3.2 – DATT setup

For the DATT experimental procedure, one layout was set for inspection, as shown in Figure 3.1. This layout was composed of two heat sources, one hot and the other cold, one IR camera and the test specimen. The hot source was displayed in reflection mode, i.e., both the heat source and IR camera were located on the same side of the sample and the cold source was displayed in transmission mode, i.e., the source and IR camera were located on opposite sides of the sample.

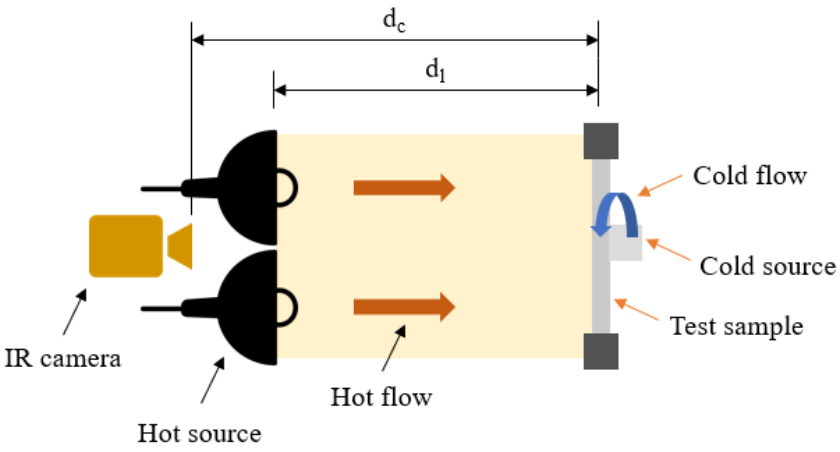

Figure 3.1 – DATT schematic experiment setup

Hot Source: For the hot flow, four Phillips IR-175C-PAR lamps of 175 W were used, bringing the total of the heat to 700 W. This group of lamps was placed perpendicular to the test specimen, at a distance of 600 mm, denoted by d_l in the scheme in Figure 3.1 and also shown in Figure 3.2.

Cold Source: The cold flow was only tested on Sample One, consisting of a box with a plain and curved side, as explained in sub-chapter 3.4 and seen in Figure 3.2. One of the sources of the cold flow was a Meech Vortex Tube with a length of flexible knuckle trunking to direct the air. This instrument was placed above the specimen, perpendicular to it, as shown in Figure 3.2 a) and b). The air flow of the vortex is around 50 l/min and, as shown in Chapter 4, the interior of the sample reached, on average, – 4 ºC. In a small group of tests, it was used the cooling fluid Redex G13, with a setup and conditions closed to the air flow but where the liquid was poured into the sample, as shown in Figure 3.2 c) and d), taking around 2-3 seconds to fill in, and remained inside the sample until the end of the experiments. With the cooling fluid, the interior of the sample reached around – 26 ºC.

IR Camera: The infrared camera used was a Fluke Ti400, which recorded the thermal response of the sample during the inspection and was placed perpendicular to the test specimen, at a distance of 800 mm, denoted by d_c in the scheme in Figure 3.1, and above the lamps, as shown in Figure 3.2 a) and c). Fluke Ti400 has a spectral range of 7.5 to 14 µm, temperature measurement range of -20 °C to +1200 °C and detector resolution of 320x240 (76,800 pixels) [49,67].

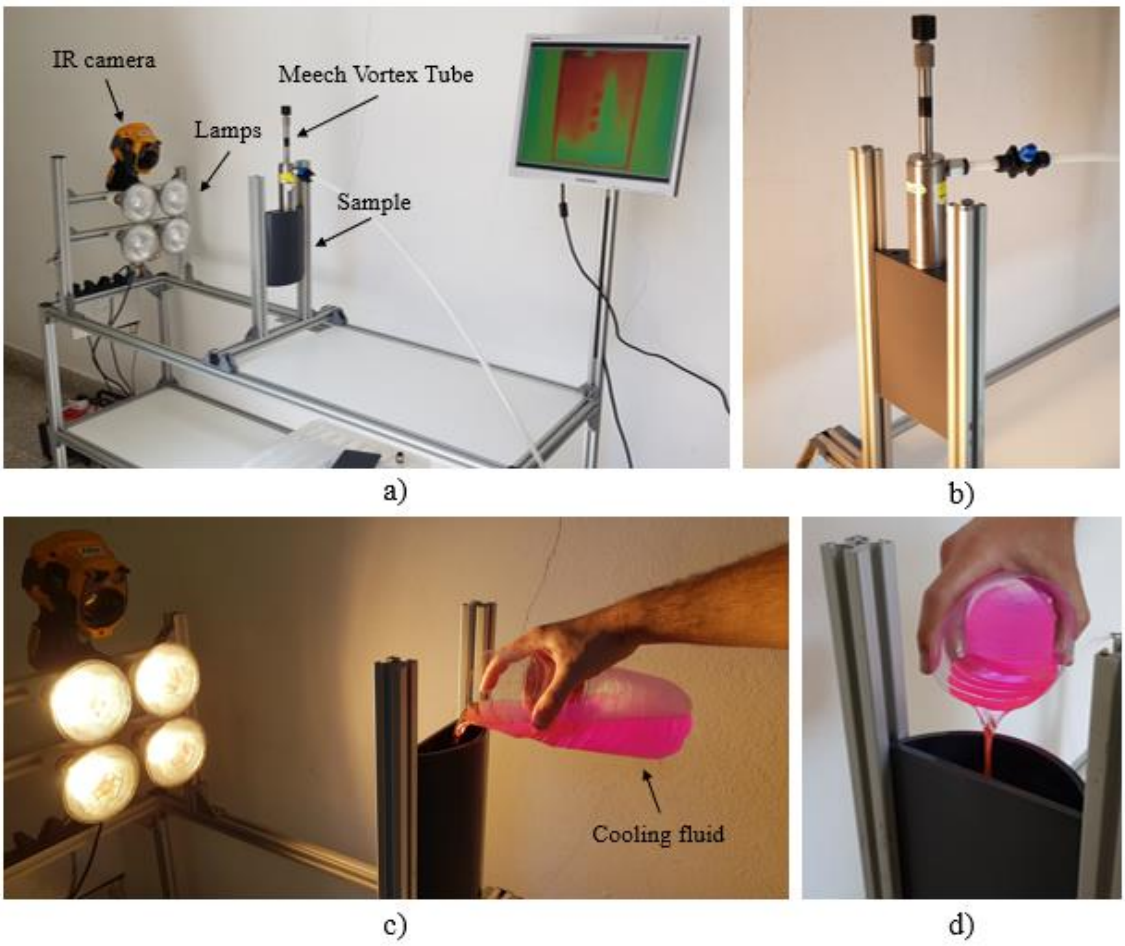

Figure 3.2 – a) DATT setup with the vortex b) Meech Vortex Tube and sample c) DATT setup with the cooling fluid d) pouring the cooling fluid into the sample.

In order to collect and process the data from the inspections, two software's were used, SmartView™, to collect the temperature points across the thermograms, and LabVIEW, to set the time of the inspection, the instant in which the lamps turn on and off and to acquire the temperature inside the sample.

3.3 – ACU equipment

For the ACU experimental procedure, a new layout was developed, using reflection mode for inspection, being both the transmitter and receiver probes placed on the same side of the sample, as shown in Figure 3.3. This layout was composed of two probes, one flaw detector and the test specimen.

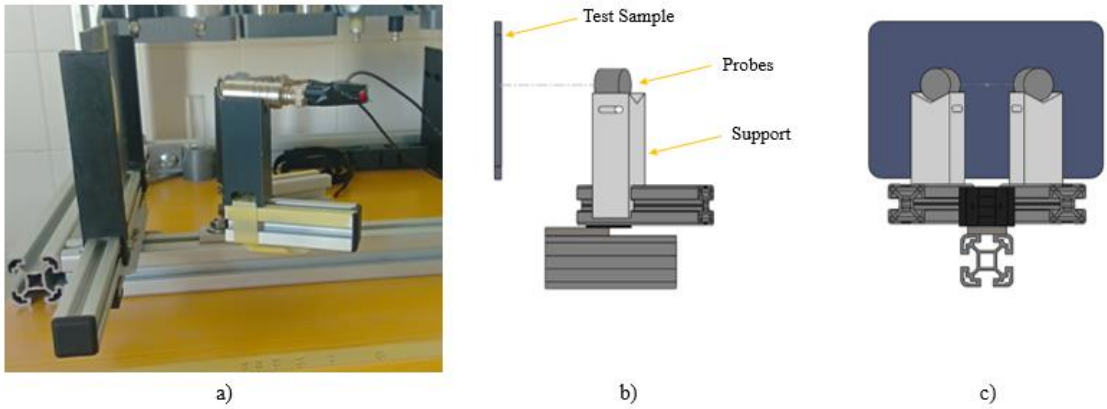

Figure 3.3 - ACU equipment a) real experiment set-up in reflection mode b) equipment used and sample c) schematic experiment set up.

Probes: It was used one pair of low frequency transducers, one transmitter and the other receiver, with frequency of 200 kHz, wavelength of 1.72 mm and piezoelectric diameter of 11 mm. These probes were placed in different angles, denoted by α, different distances to the test sample, denoted by d, and in different distances on the support, denoted by d_p in the scheme of Figure 3.4 a).

Support and structure: In order to accommodate the probes, it was designed and printed two PLA supports, which fit two aluminium Bosch Rexroth profiles and can be moved along the distance d_p. These two profiles are connected by a hinge, which allows to vary angle α, and this hinge is connected to a third aluminium Bosch Rexroth profile, enabling a wide range for distance d.

Flaw Detector: The instrument used was the STARMANS' DIO 1000 LF, suitable to inspect materials with high ultrasonic waves attenuation, such as plastic materials, shown in Figure 3.4 b).

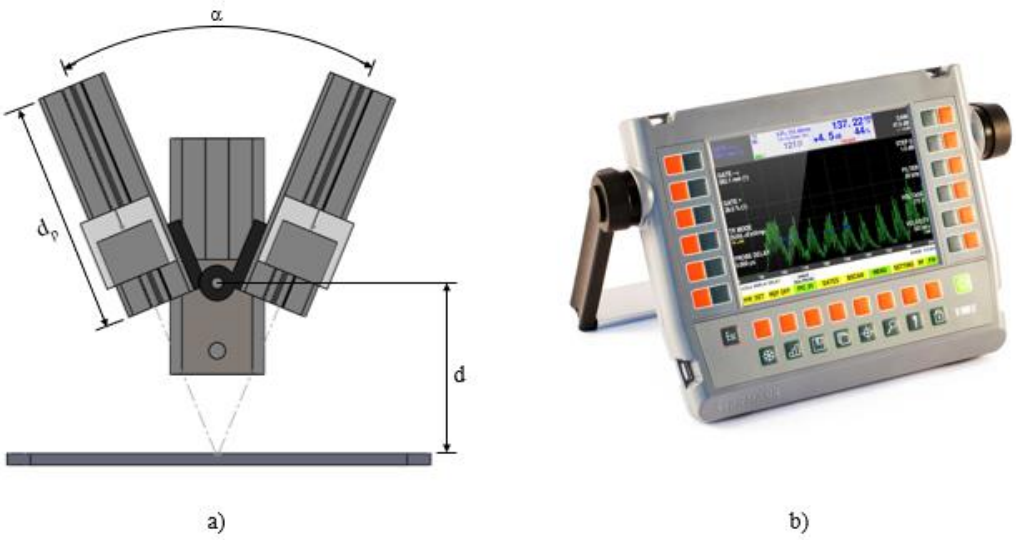

Figure 3.4 - ACU equipment a) placement of the probes b) flaw detector [68].

3.4 – Sample One

It was manufactured a grey PLA piece with a plain side (1P) and a curved side (1C), as shown in Figure 3.5. Each side of the sample has three identical square voids which simulate delaminations, with height and width of 15 mm and thickness of 0.5 mm, the full amount being six delaminations per sample. Both the plain and curved sides have a height of 200 mm, width of 150 mm and thickness of 5 mm.

The delaminations vary in depth and location in each side, as shown in Figure 3.6, being designated as:

- **Outer defect (OD)**, which is located at a height of 125 mm and depth of 0.75 mm measured by the outer wall;
- **Middle defect (MD)**, which is located at a height of 100 mm and depth of 2.25 mm measured by the outer wall;
- **Inner defect (ID)**, which is located at a height of 75 mm and depth of 4 mm measured by the outer wall.

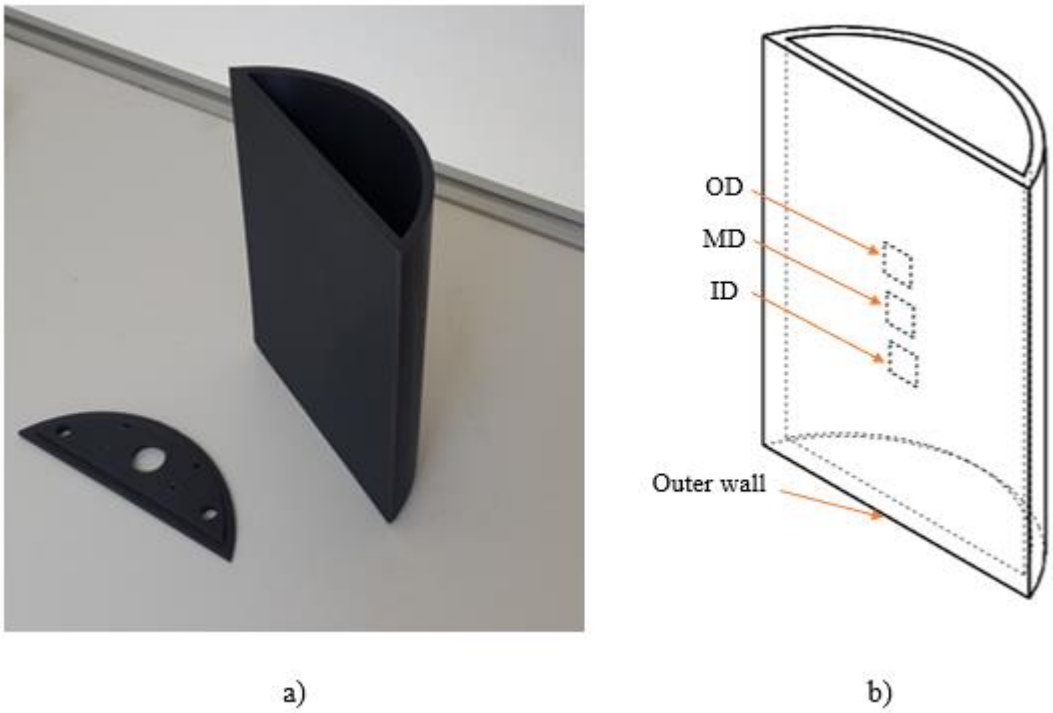

Figure 3.5 - Sample One a) printed version b) model showing the delaminations with the legend of the defects and outer wall.

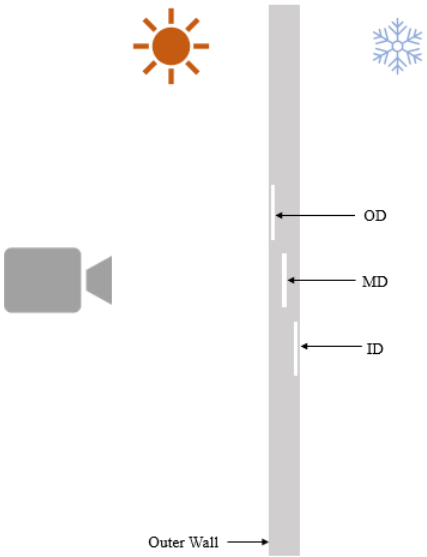

Figure 3.6 - Representation of the delaminations of plain side, regarding their depths and locations.

The sample was printed as a box with one entry because this allowed the printing of two different surfaces (1P and 1C) in order to conduct different experiments and

prevented the cold air from rapidly escaping the sample. For the latter purpose and in order to have an entrance for the cold flow, there were created two variants for a lid, one lid with a single hole, as shown in Figure 3.7, and one lid with additional holes to allow the recirculation of the air and therefore, for the sample to achieve lower temperatures, shown in Figure 3.5 a).

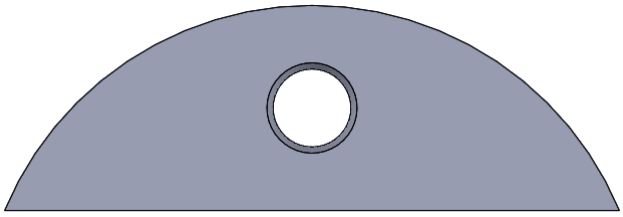

Figure 3.7 - Lid with one entrance for the cold flow.

3.5 – Sample Two

The second sample consists of a plain grey PLA piece with a height of 200 mm, width of 150 mm and thickness of 5 mm, as shown in Figure 3.8.

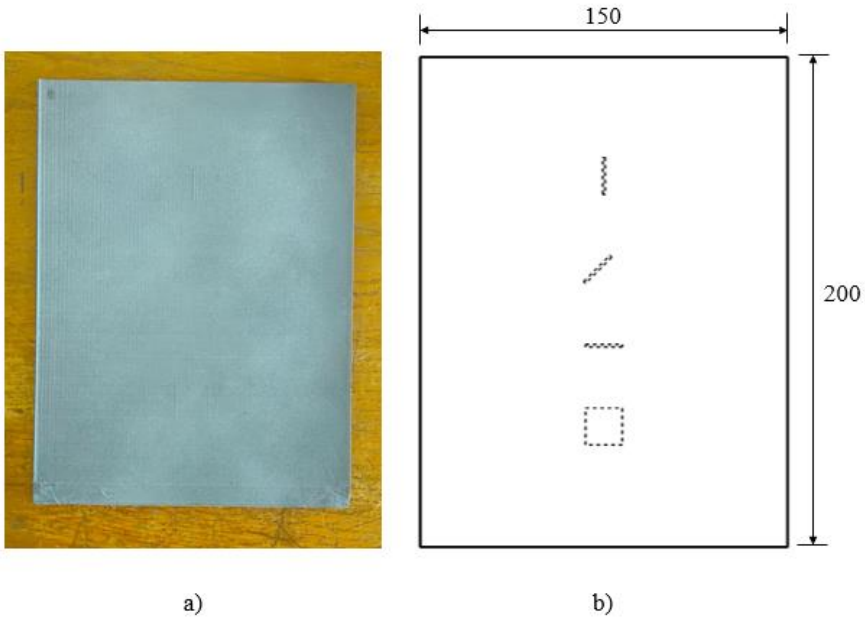

Figure 3.8 - Sample two a) printed model b) dimensions.

This sample has one square void, which simulates a delamination, with height and width of 15 mm and thickness of 0.5 mm, and three rectangular voids, that simulate

debondings, with dimensions 15 x 1 x 2 mm. All defects are displayed at different depths, locations and orientations, as shown in Figure 3.9:

- **Vertical debonding (VD)**, which is located at a height of 151.5 mm and depth of 2 mm measured by the outer wall;
- **Diagonal debonding (DD)**, which is located at a height of 113.7 mm and depth of 2 mm measured by the outer wall;
- **Horizontal debonding (HD)**, which is located at a height of 82.19 mm and depth of 2 mm measured by the outer wall;
- **Delamination (D)**, which is located at a height of 49.2 mm and depth of 1.25 mm measured by the outer wall.

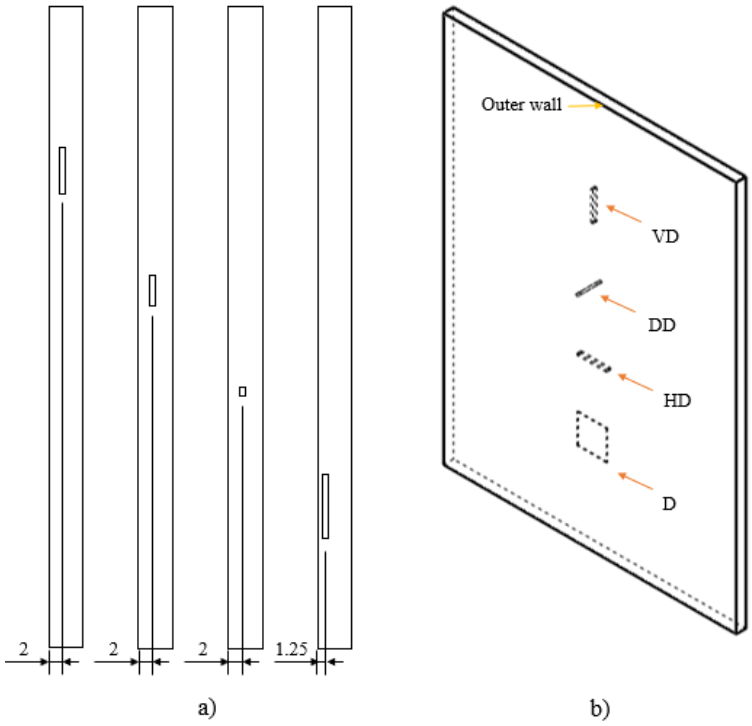

Figure 3.9 - Model of Sample two displaying the a) depth and b) position of each defect.

3.6 – Sample Three

The third sample consists of a plain grey PLA piece with a height of 120 mm, width of 180 mm and thickness of 5 mm. This sample has one rectangular void in the middle of the piece, simulating a delamination, with height of 100 mm, width of 60 mm and thickness of 0.5 mm, as shown in Figure 3.10.

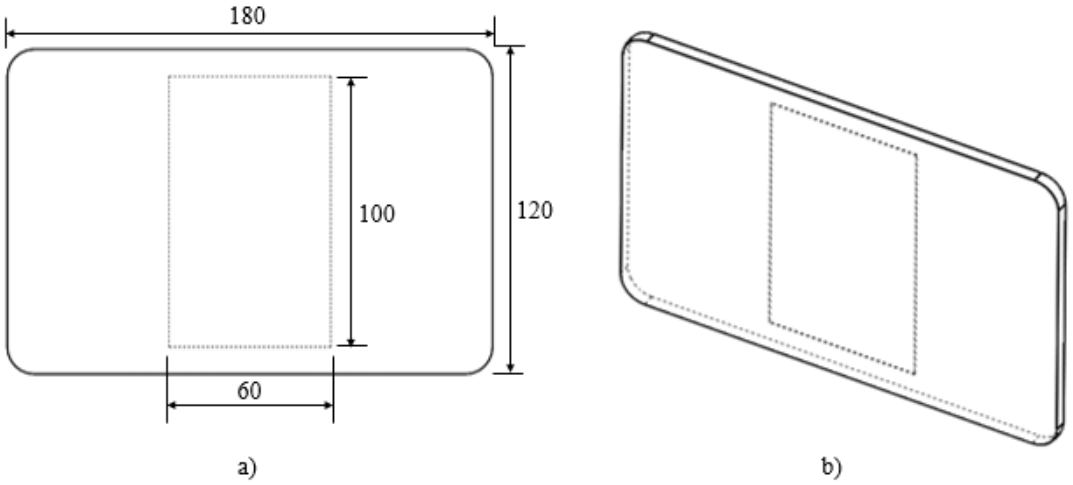

Figure 3.10 - Sample three a) dimensions b) model displaying the delamination.

3.7 – Sample Four

This sample consists of a thin plain grey PLA with a height of 120 mm, width of 180 mm and thickness of 2 mm, which has a large flat washer M12 x 3mm in the middle, as shown in Figure 3.11.

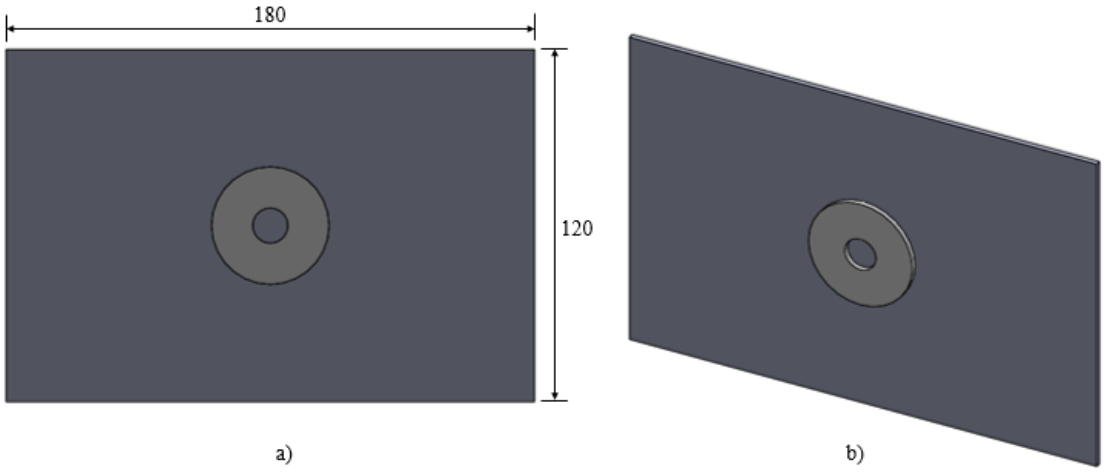

Figure 3.11 - Sample four a) dimensions b) model displaying the metal washer.

3.8 – Sample Five

The final sample used is a plain green PLA piece with a height of 80 mm and width of 210 mm. This sample has three different areas which vary in thickness, as shown in Figure 3.12:

- **Area one**, which is 75 mm wide and 2 mm thick;

- **Area two**, which is 60 mm wide and 6 mm thick;
- **Area three**, which is 75 mm wide and 4 mm thick.

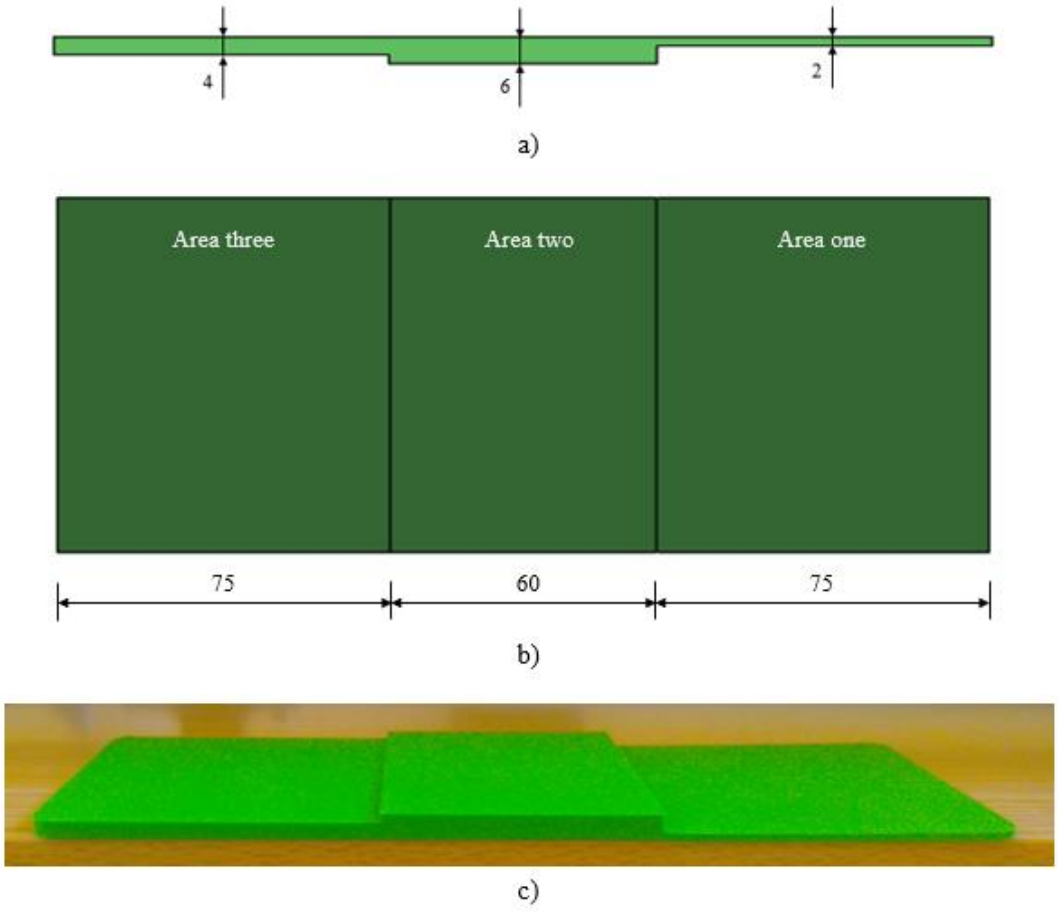

Figure 3.12 - Sample five a) thickness and b) width of each area c) printed model.

3.9 – Chapter resume

This chapter describes the Double Active Transient Thermography and Air-coupled Ultrasound equipment used and its features, and the PLA samples produced with its different defects, consisting of delaminations and/or debondings, which were inspected by the two NDT techniques.

4 – RESULTS AND DISCUSSION OF DATT CHARACTERIZATION TESTS

4.1 – Introduction

This chapter describes the experiments made with an innovative variant of the conventional active thermography, which was named *Double Active Transient Thermography* (DATT), where the evaluated object is excited by two heat sources, a cold flow and a heat flow. With these two sources, many combinations of experiments can occur, where the flows can be applied simultaneously, with delay or only one of the sources is applied. The goal of developing this technique is to be able to clearly observe with the same contrast different defects at different depths and locations.

The prior expected advantage of this technique is that, unlike LIT, which is an extremely complex variant of Active Thermography but allows the detection and position of internal defects in thickness, DATT can be a simpler and faster alternative in achieving those same results, although it depends on the thickness of the sample and needs access to both sides of the sample as it requires more than one heat source.

In this chapter, it is presented different experiments for different samples varying the cooling and heating conditions of the inspection tests. Firstly, it was recorded the temperature distribution during the heating/cooling time and acquisition time followed by the processing of the videos recorded by the infrared camera, where it was retrieved the points of temperature of the defects and free zone and calculated the temperature contrast between this points. This allowed the retrieving of the maximum temperature contrast, maximum temperature reached and respective instant of time. For the cold flow experiments, the data from the thermocouples was directly plotted into temperature charts. The parameters considered in these experiments are the instant for starting the cold flow and its duration, different defects and the influence of the lid, exposure time, curvature, and instant when the vortex is turned on.

In the experiments, the R means reference test, *i.e.* the test where only hot flow was applied, representing the conventional Active Transient Thermography.

4.2 – Sample One (1P) inspection

For this sample, there were conducted four different groups of experiments, three to determine the maximum temperature contrast and the respective time under different conditions, and one group to determine the duration and instant for the cold and heat flows that allows the visualization of the three defects at the same time:

4.2.1 – Group One

In these experiments, it was used the first variant of the lid and the compressed air was only turned on at the experiment specific time for the cold flow. There were conducted twelve different experiments, in the first six the duration of each flow was 20 s, as shown in Table 4.1, and in the last six the duration was 30 s, as shown in Table 4.2. The room temperature was, on average, 17.1 ºC.

Table 4.1 - First six experiments of Group one – 20 s.

Test Number	0 s	10 s	20 s	30 s
1	hot			
		cold		
2	hot			
			cold	
3	hot			
	cold			
4		hot		
	cold			
5			hot	
	cold			
6 (R)	hot			

Table 4.2 - Last six experiments of Group one – 30 s.

Test Number	0 s	15 s	30 s	45 s
7	hot			
		cold		
8	hot			
			cold	
9	hot			
	cold			
10		hot		
	cold			
11			hot	
	cold			
12 (R)	hot			

After the experiments, in each of the twelve videos it was retrieved nine groups of temperature values from the nine points, as shown in Figure 4.1. Then, it was calculated the average between the temperatures of points in the free zone, such as P0 and P2, P3 and P5 and between P6 and P8. Lastly, it was calculated the difference between these averages and the temperature of the near defects (points P1, P4 and P7). Figure 4.2 presents the evolution of temperature in each point, from test 1, as an example. The vertical dashed lines represent the beginning and/or ending of the flows, according to Table 4.1. From each test, it was drawn the maximum temperature contrast and respective time, as shown in Figure 4.3.

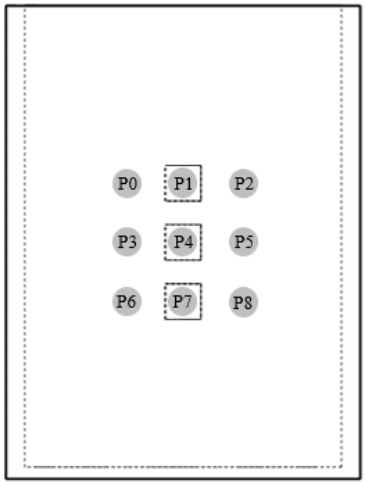

Figure 4.1 - Nine groups of temperature values from the nine points of Sample One.

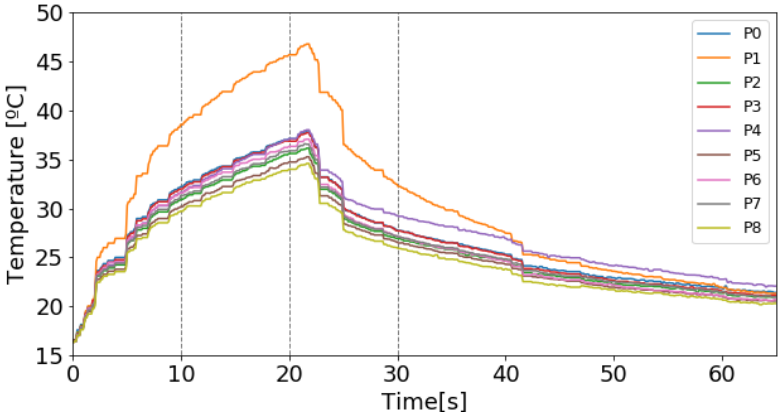

Figure 4.2 – Test 1 - evolution of temperature in each point.

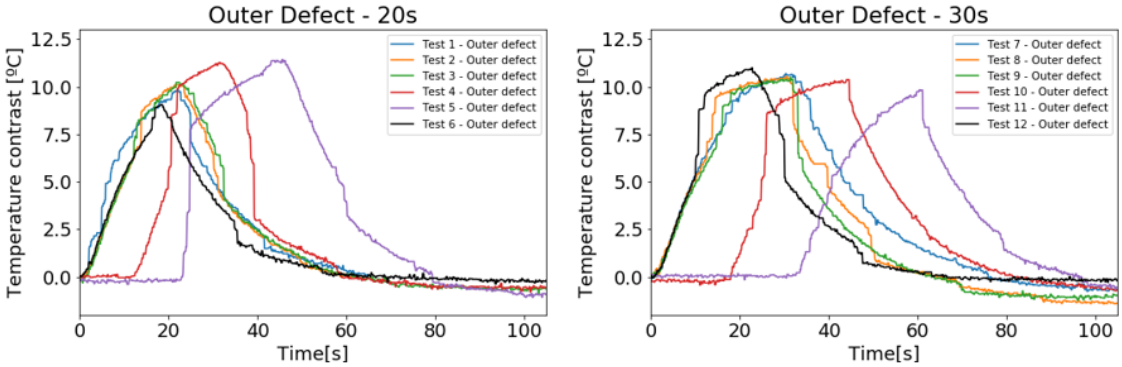

a) b)

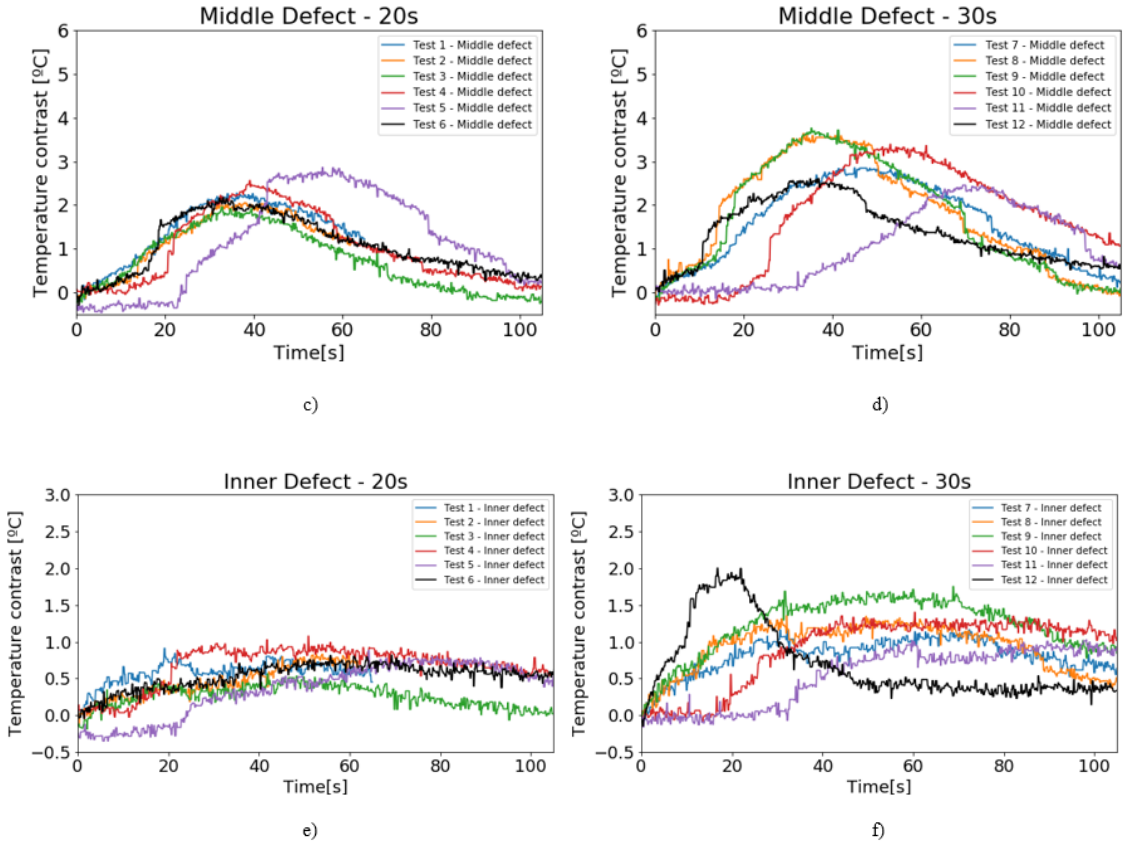

Figure 4.3 – Results of Sample 1P Group one: a) outer defect 20s b) outer defect 30s c) middle defect 20s d) middle defect 30s e) inner defect 20s f) inner defect 30s.

In this first group, the OD is the defect with higher contrasts and the maximum contrast appears near the end or immediately after the hot flow, in all tests. In Group One - 20 s tests, the reference test (test 6) has a maximum contrast of 9 ºC at around 18 s but the tests with cold flows have higher contrasts, ranging between 9.8 and 11.4 ºC, but with higher instants (tests 1, 2 and 3 reach the maximum peak at around 21s). In Group One - 30 s tests, the reference test (test 12) has a higher maximum contrast, around 11 ºC at 23 s, than the others, which range between 9.8 and 10.7 ºC, with the best instants being at 31 s for tests 7, 8 and 9.

Regarding MD, in Group One - 20 s tests, test 5 has better contrast of 2.9 ºC but worst instant (56 s), when compared to the other tests, between 2 and 2.7 ºC, at around 32 – 39 s; the Group One - 30 s tests have better contrasts, especially tests 8 and 9, with maximum contrasts close to 3.6 ºC, as opposed to the reference, with 2.6 ºC at 36 s. The maximum contrasts of MD in each test appeared 10 to 15 s after the end of the hot flow.

For the ID, in Group One - 20 s tests, test 4 provides the best contrast, with maximum of 1.1 ºC at 51 s and in Group One - 30 s tests, as the hot flow has more time to reach this defect, the contrasts are slightly higher, especially for test 12, with 2 ºC at 16.8 s, compared with the other tests, ranging between 1 and 1.7 ºC at 30.6 – 98 s.

All the defects are visible through the IR camera, but not at the same time nor with close contrast temperatures. These results have high noise and lack some consistency, mainly due to the type of lid, which without the additional holes, prevented the circulation of the air and so, the samples didn't cool down as much as the following group.

4.2.2– Group Two

In these experiments, it was used the second variant of the lid (which has additional holes to allow the recirculation of the air, enabling the sample to achieve lower temperatures) and the compressed air was only turned on at the experiment specific time for the cold flow. There were conducted six different experiments in which the duration of each flow was 30 s, the same as shown in Table 4.2. The room temperature was, on average, 17.3 ºC.

After the experiments, the same procedure was made as in Group One. Figure 4.4 presents the evolution of temperature in each point, from test 9, and the vertical dashed line represents the ending of the cold and hot flows from that test, according to Table 4.2. In all tests from this group, the chronometer started counting 20 s before the beginning of the experiment and from each test, it was drawn the maximum temperature contrast and respective time, as shown in Figure 4.5.

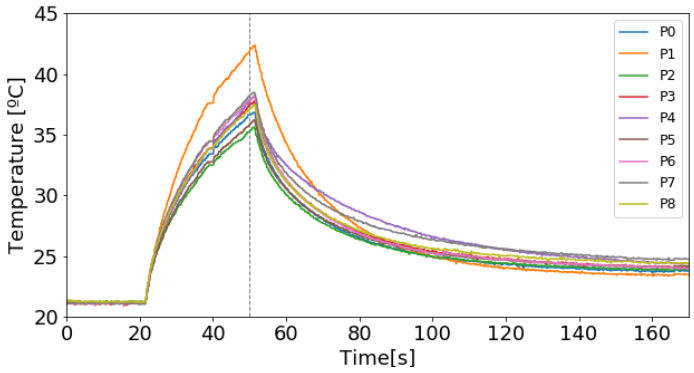

Figure 4.4 – Test 9 – evolution of temperature in each point.

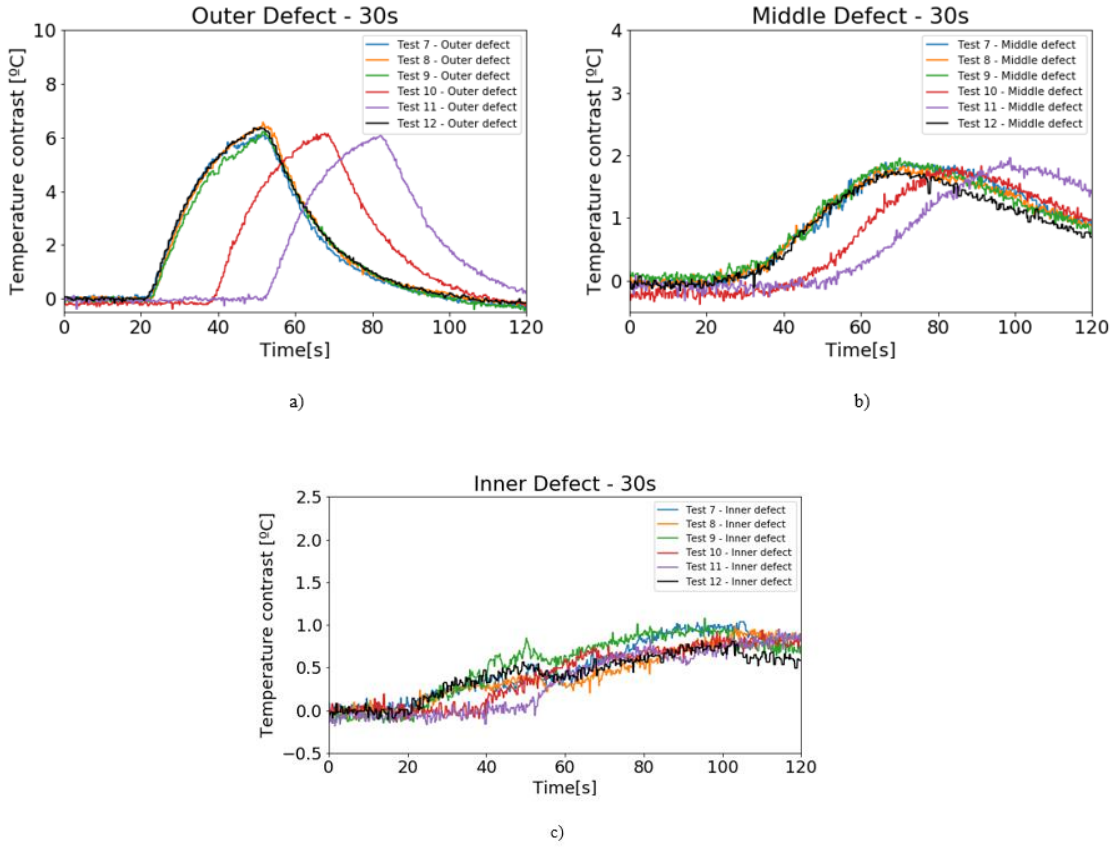

Figure 4.5 - Results of Sample 1P Group two: a) outer defect 30s b) middle defect 30s c) inner defect 30s.

When compared to the previous group, these results have less noise, especially the outer defect. In the OD, the maximum contrast doesn't differ widely across the tests, with contrasts between 6.1 to 6.6 ºC and the lowest contrasts being to tests 10 and 11 (hot flow delay). In all tests, these maximum contrasts appear near the end or immediately after the hot flow.

The same can be concluded with the MD, with maximum contrasts between 1.8 and 2 ºC, at instants between 46 and 78 s, slightly higher than the reference, with 1.7 ºC at 46 s. These peaks usually occur 15 to 20 s after the end of the hot flow.

In the ID, most tests with cold flow have higher contrasts than the reference test (0.81 at 75s), especially tests 7 and 9, at around 1 ºC with 84 and 75 s, respectively.

These results provide a clearer idea of the influence of the cold in each defect, since all defects are visible, even if not at the same time, and the majority of the tests with both

cold and hot flows provide better contrasts than the reference test (only hot flow), unlike the previous group.

4.2.3 – Group Three

In these experiments, it was used the second variant of the lid and the compressed air was previously turned on before the experiment (10s to 15s before), in order to stabilize the flow and temperature, and then connected to the lid at the experiment specific time for the cold flow. There were conducted eight different experiments, in which the duration of each flow was 20s, as shown in Table 4.3. The room temperature was 19.3 ºC.

Table 4.3 - Experiments of Group three – 20 s.

Test Number	0 s	10 s	20 s	30 s	40 s
1	hot	cold			
2	hot		cold		
3	hot			cold	
4	hot	cold			
5		hot			
	cold				
6			hot		
	cold				
7				hot	
	cold				
8 (RQ)	hot				

After the experiments, the same procedure from Group one was applied. Figure 4.6 presents an idea of the evolution of temperature in each point, from test 3, as an example. The vertical dashed lines represent the beginning and/or ending of the flows, according to Table 4.3, the chronometer started counting 10 s before the beginning of the experiment. From each test, it was drawn the maximum temperature contrast and respective time, as shown in Figure 4.7.

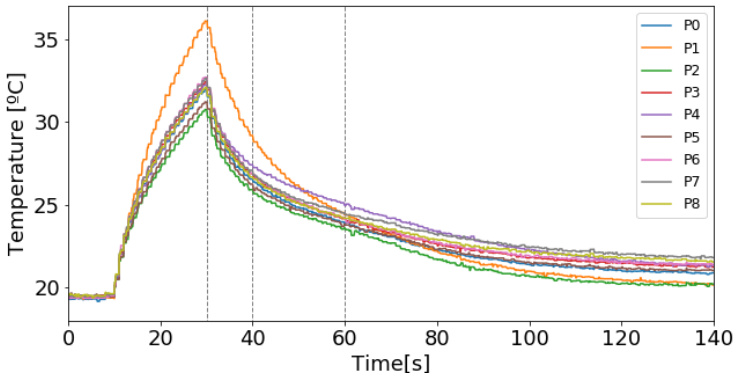

Figure 4.6 – Test 3 - evolution of temperature in each point.

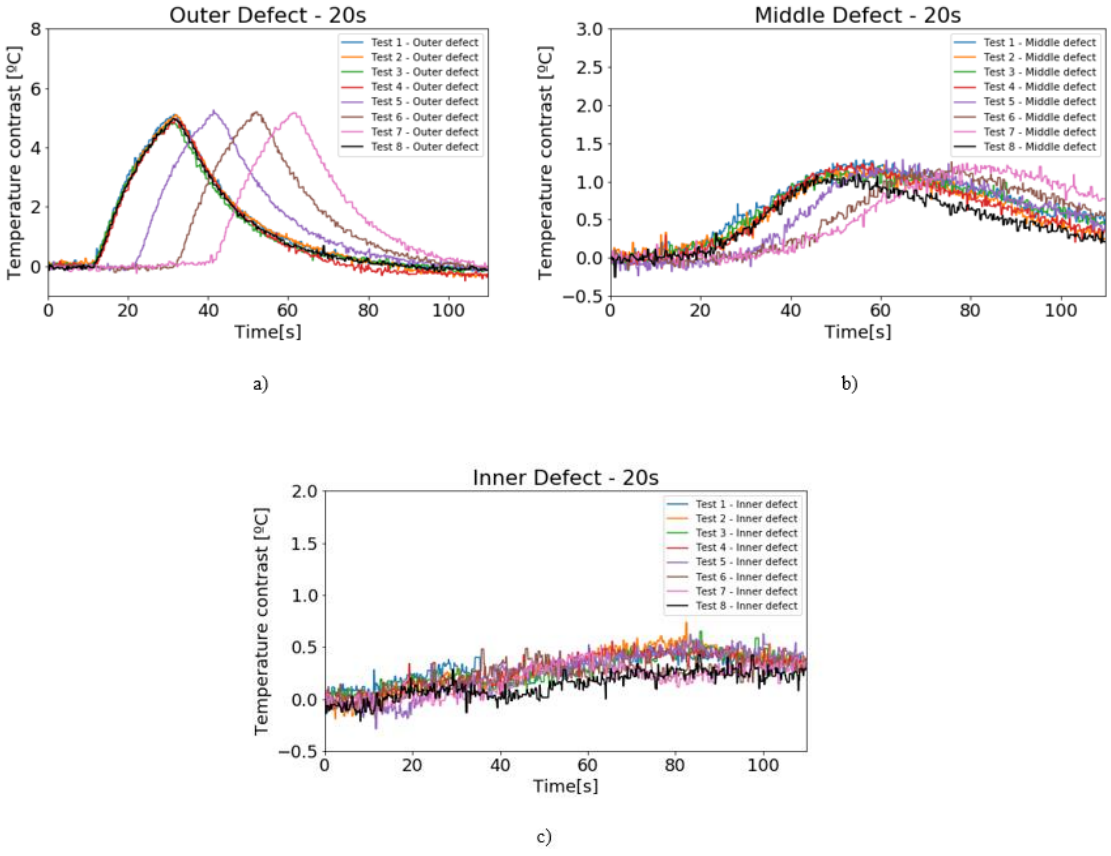

Figure 4.7 - Results of Sample 1P Group three: a) outer defect 20s b) middle defect 20s c) inner defect 20s.

In these experiments, it can be concluded that for tests with 20 s of duration for each flow, with a lid with various holes and the vortex being previously turned on, OD doesn't

benefit from the introduction of cold, as the maximum contrast remains close to 5 ºC and occurs always after the end of the hot flow.

The same can be concluded for the MD, in which the maximum contrast is around 1.2 ºC for every experiment with cold and hot flows (slightly higher than the reference, with 1.1 ºC at 45s) and occurs 30s after the end of hot flow in experiments with cold flow delay (tests 1, 2 and 3) and 20s after the end of hot flow in experiments with hot flow delay (test 5, 6 and 7), both flows at the same time (test 4) or just hot flow (test 8).

However, ID benefits from the introduction of the cold flow. As seen in Figure 4.8, results from tests 2, 3 and 4 have greater maximum contrast (0.73, 0.65 and 0.56, respectively) when compared to the application of only hot flow (0.43), even considering the initial temperature contrast mismatch.

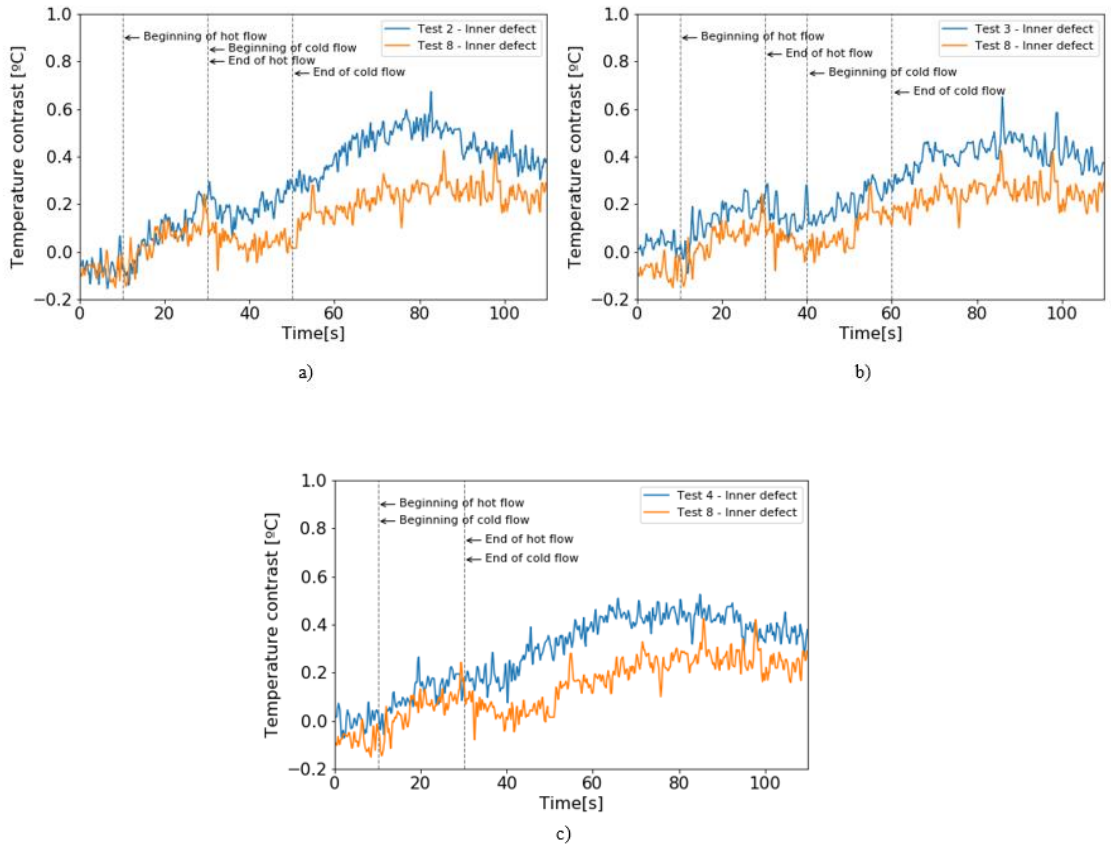

Figure 4.8 – Comparison between DATT and conventional APT a) Tests 2 and 8 b) Tests 3 and 8 c) Tests 4 and 8.

As also seen in Group Two, the inner defect can be seen slightly better with the introduction of the cold. Comparing with the results from the 20 s tests of Group One, the OD, MD and ID have 1.8, 3.3 and 1.4 times better contrasts than the ones from these group.

4.2.4– Group Four

In these experiments, it was used the second variant of the lid and the compressed air was only turned on at the experiment specific time for the cold flow. There were conducted two different experiments with different flow times, as shown in Table 4.4, to better understand the instant in which all three defects appear at the same time. The room temperature was, on average, 17.1 ºC.

Table 4.4 - Experiments of Group four.

Test Number	0 s	10 s	20 s	30 s	40 s	50 s	60 s	70 s	80 s
1					hot				
	cold								
2					hot				
	cold								

After the experiments, the same procedure from Group one was applied. Figure 4.9 presents the evolution of temperature in each point, from test 2, as an example. The vertical dashed lines represent the beginning and/or ending of the flows, according to Table 4.4, and the chronometer started counting 10 s before the beginning of the experiment. From each test, it was drawn the maximum temperature contrast and respective time, as shown in Figure 4.10.

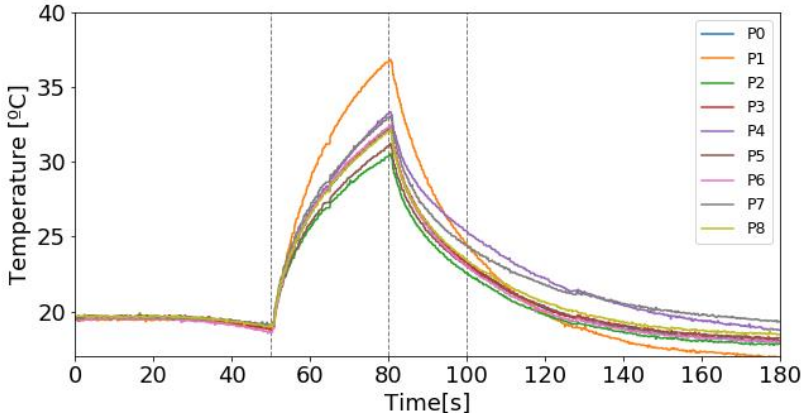

Figure 4.9 – Test 2 – evolution of temperature in each point.

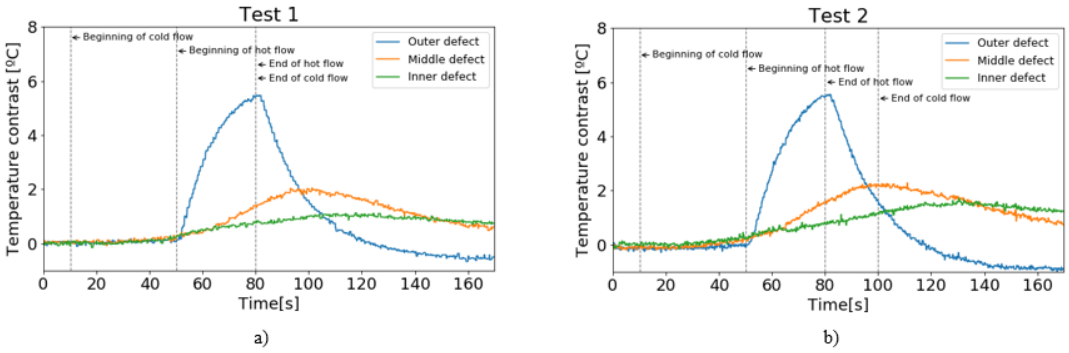

Figure 4.10 – Results of Sample 1P Group four: a) test 1 b) test 2.

It can be concluded that the outer and middle defect do not benefit from the introduction of the cold flow (as also concluded in Group Three), with around 5 ºC for the OD and around 2 ºC for the MD. In contrast, the inner defect has 1.13 ºC of maximum contrast at 75 s in test 1 and 1.7 ºC at 107 s in test 2, values that are higher than those obtained in the previous groups (apart from the reference test of Group One), although the duration of the cold flow is higher in these tests (from 20 and 30 s to 70 and 90 s).

In test 1, the instant in which all three defects appear at the same time with close temperature values is around 87 s (37 s after the beginning of the hot flow), with temperature values between 25 and 27 ºC, as shown in Figure 4.11 a). In test 2, the instant in which all three defects appear at the same time with close temperature values is around 88 s (38 s after the beginning of the hot flow), with temperature values between 25 and 26 ºC, as shown in Figure 4.11 b). As comparison, in Figure 4.12, it is shown three instants from Test 8 of Sample 1P Group Three (reference test where it is applied only

the hot flow) where the defects are visible. It can be noticed the importance of introducing the cold flow to better visualize the three defects at approximately the same time. However, there is no great difference between the tests regarding the best instant to see all three defects at the same time.

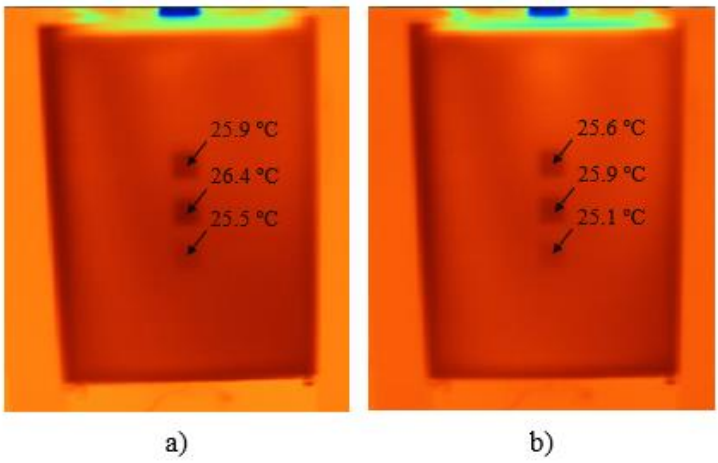

Figure 4.11 - Sample 1P Group four thermograms where all three defects appear at the same time a) 37 s after the beginning of the hot flow for test 1 b) 38 s after the beginning of the hot flow for test 2.

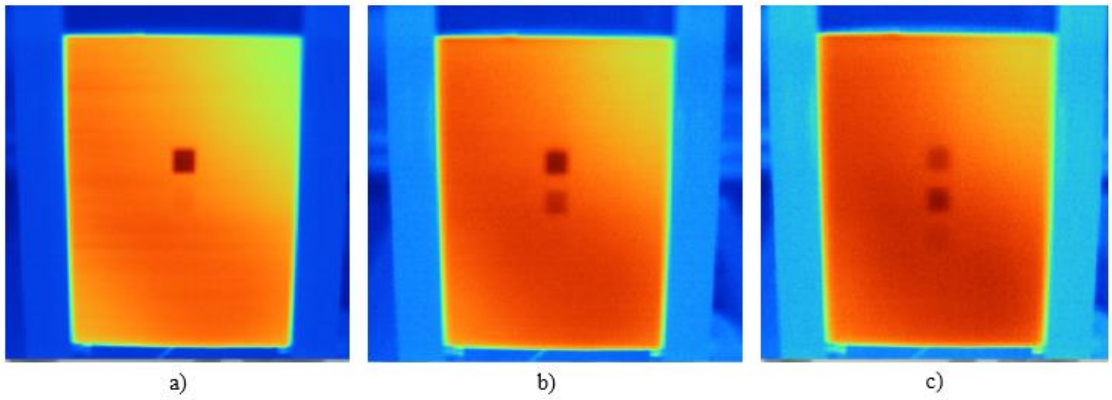

Figure 4.12 – Sample 1P Group three thermograms (reference test – hot only): a) instant of 21 s where the outer defect has the higher contrast b) instant of 36 s where the outer and middle defect can be seen c) instant of 50 s where the three defects can hardly be seen.

4.3 – Sample One (1C) inspection

There were conducted twelve different experiments, identical to Group one, in which the first six the duration of each flow was 20 s, as shown in Table 4.1, and in the last six

the duration was 30 s, as shown in Table 4.2. The room temperature was, on average, 19.7 ºC.

After the experiments, the same procedure from Sample 1P Group one was applied. Figure 4.13 presents the evolution of temperature in each point, from test 5, as an example. The vertical dashed lines represent the beginning and/or ending of the flows, according to Table 4.1, and the chronometer started counting 20 s before the beginning of the experiment. From each test, it was drawn the maximum temperature contrast and respective time, as shown in Figure 4.14.

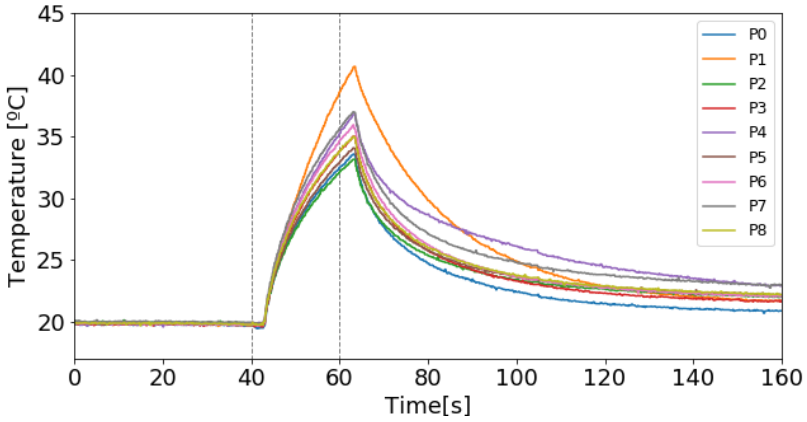

Figure 4.13 - Test 5 - evolution of temperature in each point.

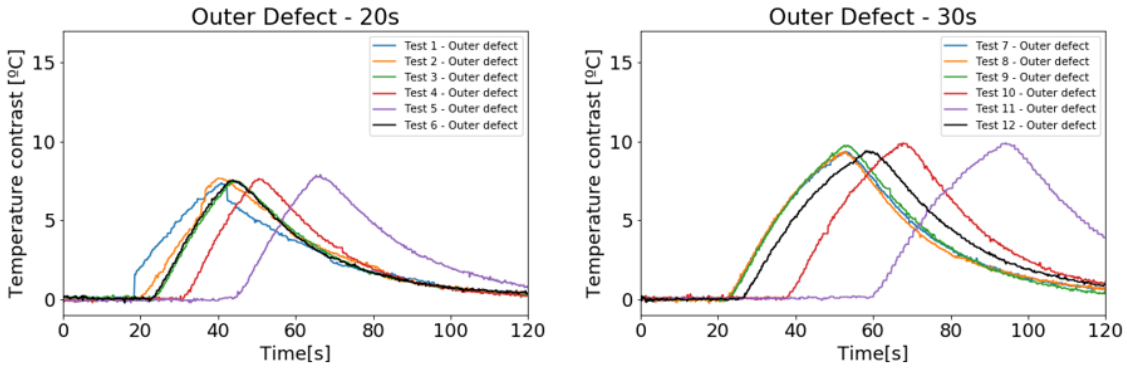

a) b)

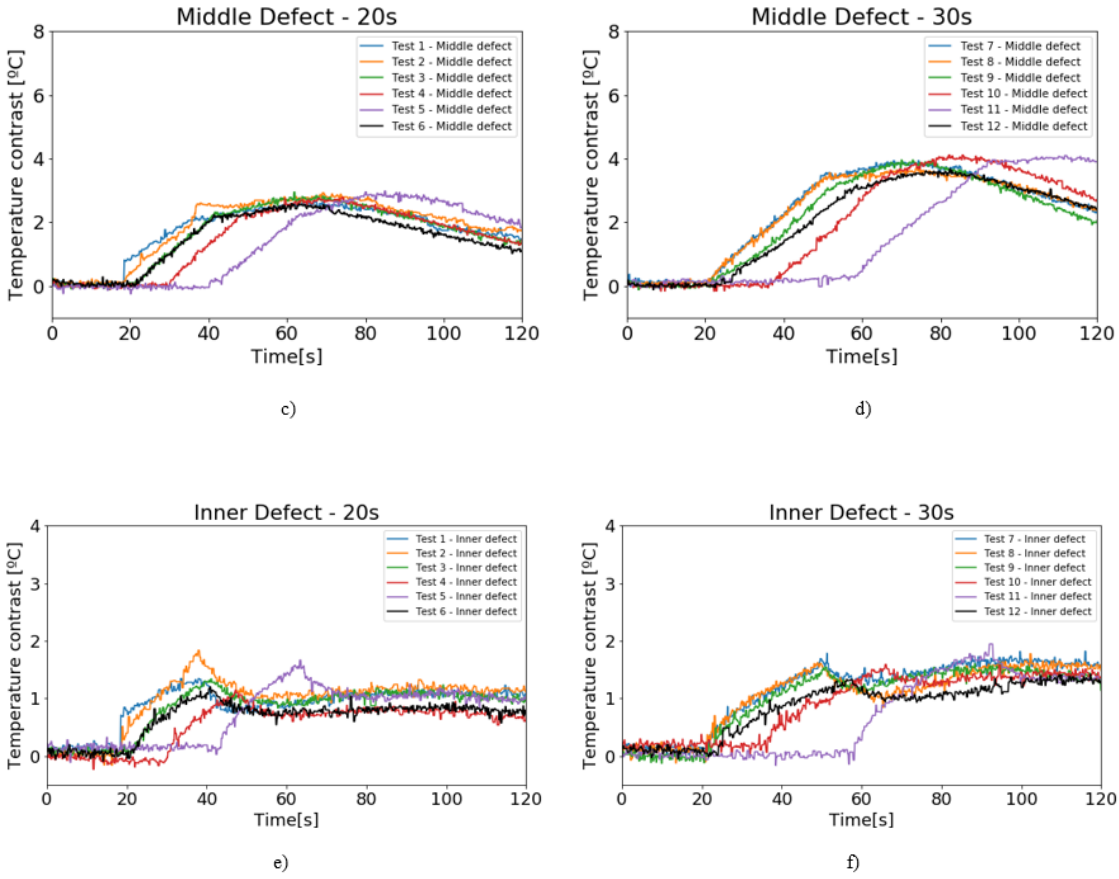

Figure 4.14 - Results of Sample 1C: a) outer defect 20s b) outer defect 30s c) middle defect 20s d) middle defect 30s e) inner defect 20s f) inner defect 30s.

Regarding the OD, in the 20 s tests, the maximum contrast doesn't differ across the tests, with contrasts around 7 ºC. Tests 1 and 2 have slightly better instants, 20 and 21 s, respectively, than the reference, 23 s. In the 30 s testes, the contrasts are constant but higher, at 10 ºC, and tests 7, 8 and 9 have better instants, around 32 s, comparing with the reference, 38 s. In all tests, these maximum contrasts appear near the end or immediately after the hot flow.

In the 20 s tests of MD, contrasts vary between 2.6 and 3 ºC, and tests 2, 3 and reference have the best instants, between 41 and 49 s; in the 30 s tests, all tests with cold have slightly better contrasts than the reference, around 4 ºC opposed to 3.7 ºC, and test 9 has the best instant of 50 s.

In the 20 s tests of ID, tests 2 has higher maximum contrast and better instant, 1.8 ºC at 38 s, in the 30 s tests, test 7, 8 and 9 have higher maximum contrasts, between 1.6 and

1.8 ºC at around 80 s. In general, tests with cold delay or hot and cold flows simultaneous provide better results than the reference, for the inner defect.

It can be concluded, as could also be seen in Group One, that higher exposure time provides around 1.5 times higher maximum contrasts for OD and MD. Once again, the outer and middle defect visibility has not improved with the introduction of the cold flow.

4.4 – Cold flow experiment with air (Sample One)

In this experiment, there were conducted two different groups of experiments, the first one to understand the minimum temperature that the sample reaches when subjected to a cold flow from the vortex and the last one to understand the effect of previously turning on the cold flow before the experiments:

4.4.1 – Group One

In these experiments, it was used the second variant of the lid (which has additional holes to allow the recirculation of the air, enabling the sample to achieve lower temperatures) and it was studied the behaviour of the cold flow in four different locations of the Sample One, as shown in Figure 4.15 a):

- T1 is located on the upper left side of the sample;
- T2 is located on the upper right side of the sample;
- T3 is located at the entrance of the cold flow;
- T4 is located in the middle of the bottom of the sample.

The temperature variation results are shown in Figure 4.15 b). It is important to note that there is a mismatch of 2 ºC between the room temperature and the temperature indicated by the thermocouples. The room temperature was, on average, 19.5 ºC and the cold flow lasted 74 s. Areas T1, T2 and T4 reached minimum temperatures of around -4 ºC, respectively, in approximately 63 s, and area T3 reached -18.8 ºC in 48 s.

On average, it takes 63 s for the inside of the sample to reach the minimum temperature, compared to the reference test (test 8 of Group three), where it reaches the maximum temperature at around 20.4 s.

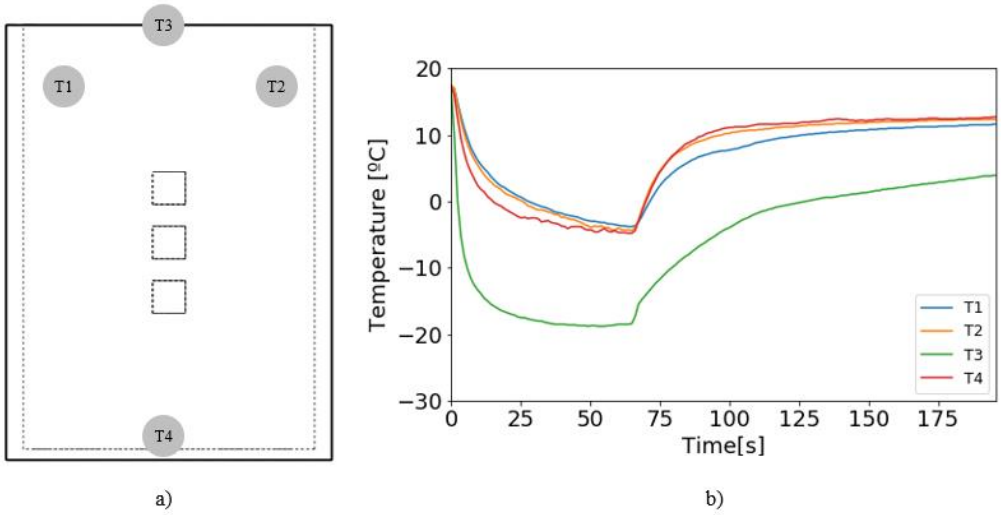

Figure 4.15 - Group one cold flow experiment a) areas measured b) temperature variations across the four areas.

4.4.2– Group Two

In these experiments, it was used the second variant of the lid and it was studied the effect of turning on the cold flow 10 s and 30 s before the beginning of the experiments, as shown in Table 4.5. The temperature variation results can be seen in Figure 4.16. The room temperature was 19.3 ºC.

In test 1, areas T1, T2 and T4 reached minimum temperatures of around -4.5 ºC, respectively, in approximately 17 s, and area T3 reached -22.6 ºC in 18.9 s.

In test 2, areas T1, T2 and T4 reached minimum temperatures of around -7.8 ºC, respectively, in approximately 17 s, and area T3 reached -23.7 ºC in 15.4 s.

Table 4.5 - Experiments of Group two.

Test Number	10 s	20 s	30 s	40 s	50 s
1	Vortex				
		Cold			
2	Vortex				
				Cold	

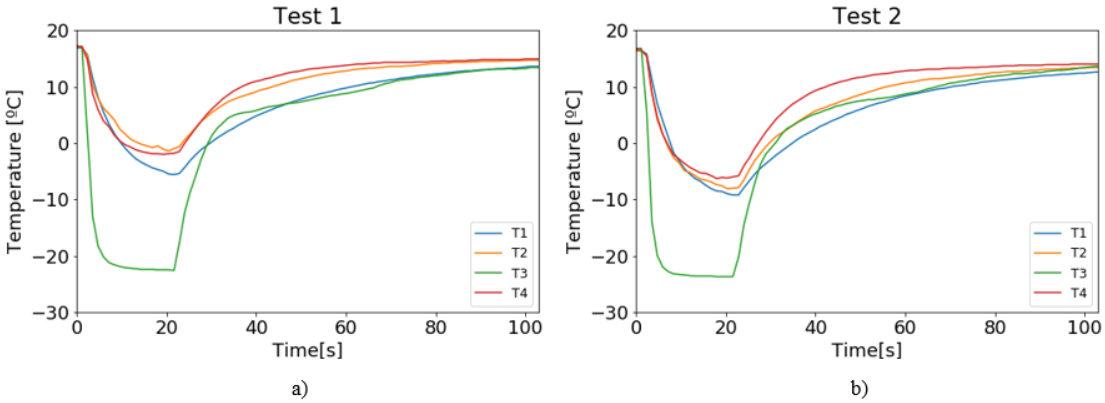

Figure 4.16 - Temperature variation results a) test 1 b) test 2.

It can be concluded that turning on the compressed air before beginning the experiment provides lower temperatures, compared to Group one, especially inside the sample. This improvement reflects the increase of maximum contrast of the ID in Group Three of Sample 1P.

4.5 – Experiment with cooling fluid Regex G13 (Sample One)

Additionally, there were conducted five different experiments with cooling fluid, instead of air, as shown in Table 4.6. As mentioned in Chapter 3, the liquid remained inside the sample until the end of the experiments, explaining why Table 4.6 does not provide an end time, as it depends on the duration of its test, which is shown in the results presented in Figure 4.17. Figure 4.17 a) shows the evolution of temperature inside the sample across the four points from Figure 4.15 a).

Table 4.6 - Experiments with cooling fluid.

Test Number	-20 s	-10 s	0 s	10 s	20 s	30 s	40 s	…
1			hot					
2			hot					
			cold					
3			hot					
					cold			
4			hot					
	cold							
5			cold					

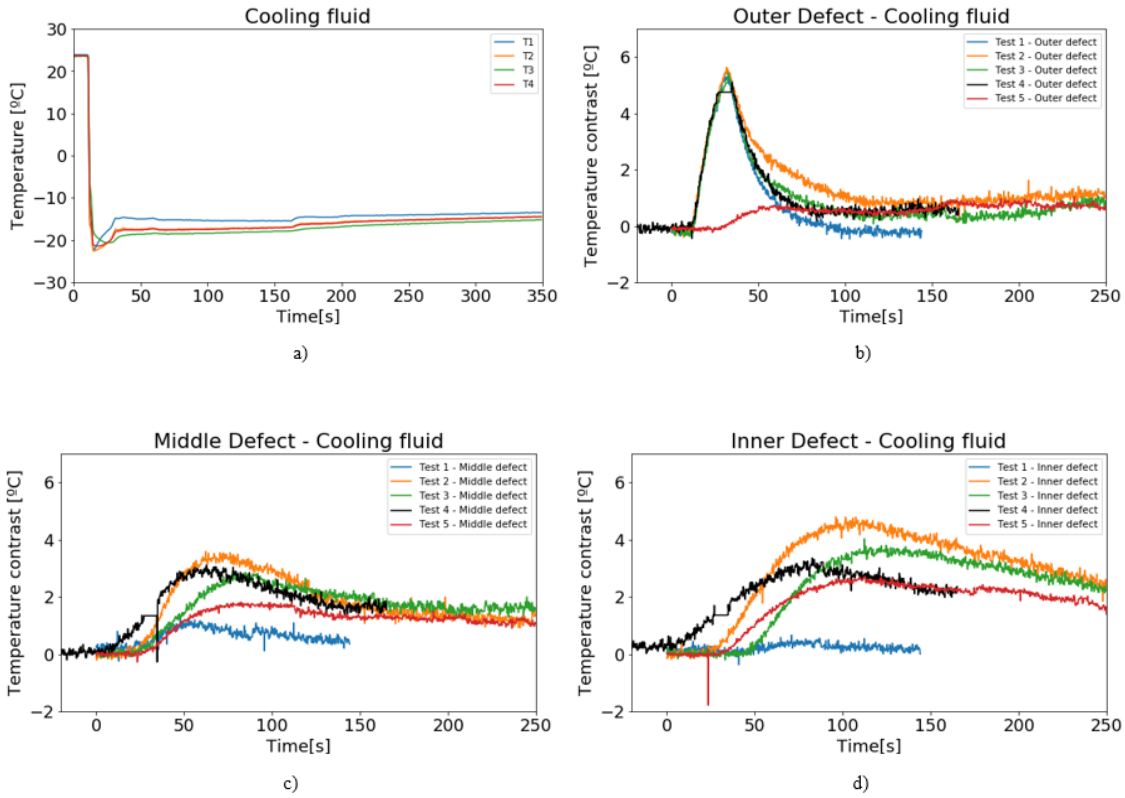

Figure 4.17 - Results of experiments with cooling fluid: a) temperature variation b) outer defect c) middle defect d) inner defect.

With the cooling fluid, all four areas of the sample reached close minimum temperatures, unlike with air, at around the same time (about 20 s). With the air flow turned on 10 s before the experiment, the sample reaches – 4 ºC, on average, but using the cooling fluid, the sample reaches between – 23 and – 26 ºC, 6.5 times colder than air, even when turning it on 30 s before.

In the OD, the highest maximum contrast of 5.6 ºC, at 31 s, is achieved in test 2. The visibility of OD has hardly improved by the introduction of the cold flow, compared with the reference test (test 1), but applying only this type of flow affects immensely the results, as seen from test 5.

In the MD, test 2 provides also the highest maximum contrast, 3.3 ºC at 63 s, which, in general, is higher than the ones obtained in the previous group, apart from tests 8 and 9 of Group One (around 3.6 ºC at 33 – 35 s).

Again, in the ID, test 2 provides the best results, around 4.8 ºC at 101 s. This result is 2.8 times better than the best result achieved with the air flow, which is 1.7 ºC at 107 s in test 2 of Sample 1P Group Four and also in test 9 of Sample 1P Group One.

Overall, the conditions of test 2 (hot and cold simultaneously) provide better temperature contrasts for the middle and inner defects, which also happened with the air flow in groups 1, 2 and 3 of Sample 1P, and indicates that there's an advantage in using hot and cold flows, rather than just hot or cold. For the first time, comparing with all previous groups of tests, all three defects are shown in a close range of contrast temperatures.

One disadvantage of this variant, compared to the air flow, is that the liquid cannot be removed after the end of the experiment. With hot and cold air flows, after each experiments, the temperature of the sample needs to return to room temperature before performing another test, but with cooling liquid, additional steps need to be taken, for instance, remove the sample from the support, in order to remove the liquid before letting the temperature of the sample return to the ideal temperature. However, since the inner defect is better visualized when turning on previously the vortex, additional steps need to be taken with the air flow in order to achieve good results with the contrasts, which is not necessary with the cooling liquid and in addition, provides even better contrasts.

4.6 – Sample Two inspection

For this sample, there were conducted two experiments where it was applied just a hot flow, as shown in Table 4.7. The room temperature was 21.3 ºC. It is important to mention that, unlike Sample 1, this sample was inspected in the horizontal, which means that the defects were not on top of but alongside each other, at equal locations, as shown in Figure 4.18 b).

Table 4.7 - Experiments of Sample two.

Test Number	0 s	10 s	20 s
1	hot		
2	hot		

After the experiments, the same procedure from Group one was applied but with twelve points, instead of nine, as shown in Figure 4.18 a). Figure 4.19 presents the

evolution of temperature in each point, from test 1, as an example. The vertical dashed line represents the ending of the hot flow, according to Table 4.7, and the chronometer started counting 5 s before the beginning of the experiment. From each test, it was drawn the maximum temperature contrast and respective time, as shown in Figure 4.20.

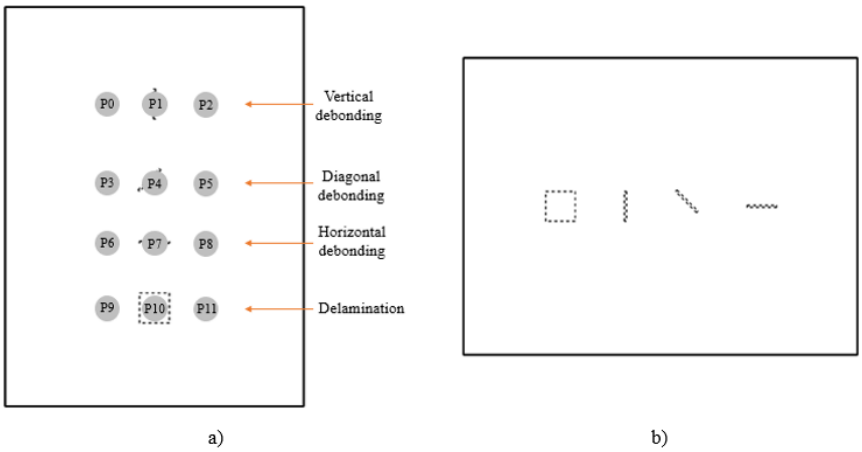

Figure 4.18 - Twelve groups of temperature values from the twelve points of Sample two.

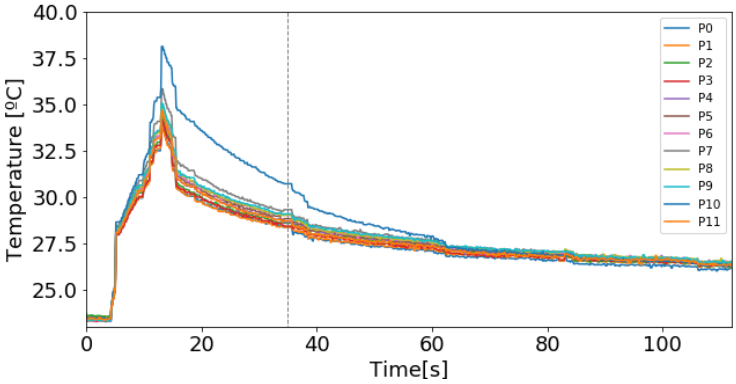

Figure 4.19 – Test 1 - evolution of temperature in each point.

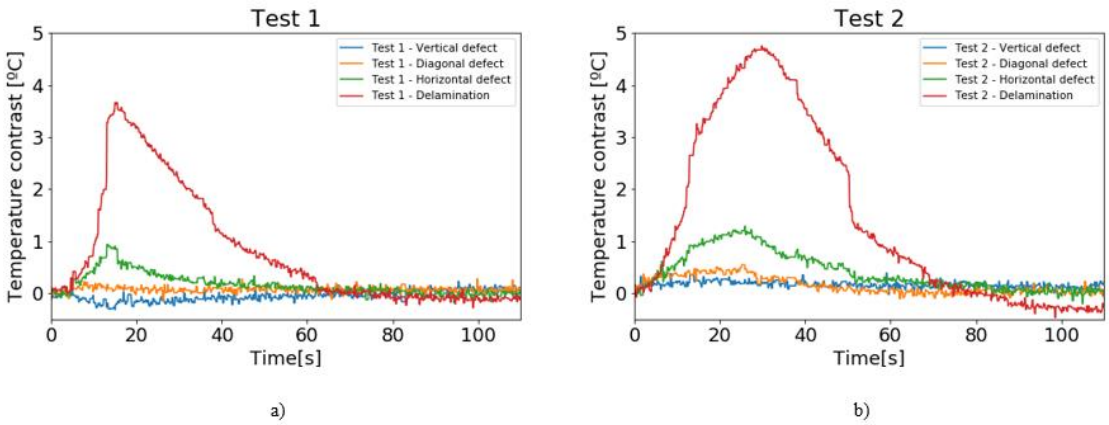

Figure 4.20 - Results of Sample 2: a) test 1 b) test 2.

The delamination has maximum contrasts of 3.7 ºC, at 10 s, and 4.8 ºC, at 55 s, for tests 1 and 2, respectively. The debondings have smaller maximum contrasts: for test 1, VD has 0.2 ºC at 90 s, DD has 0.3 ºC at 95 s and HD has 0.9 ºC at 8 s; for test 2, VD has 0.4 ºC at 54 s, DD has 0.6 s at 20 s and HD has 1.3 ºC at 21 s.

The exposure time influences slightly the contrasts but seems to significantly improve the maximum contrasts' instant, although there is a bit of noise in the data and it may prove not true in future experiments. With the debondings at a distance of 2 mm from the surface, varying its position has influence in their contrasts, for instance, the denominated horizontal debonding, which was positioned in the vertical during the inspection, has 4.5 times higher maximum contrast in test 1 and 3.3 times in test 2, comparing with the vertical debonding (placed in the horizontal).

4.7 – Chapter resume

This chapter describes the results and discussion of the two samples evaluated by the DATT technique. When not allowing the recirculation of the air inside the sample, as happens in Group One of Sample 1P, the reference test, *i.e.* conventional Pulsed Active Thermography, provides the best results for the outer and middle defects, in general. However, by using a lid that allows the recirculation of the air and turning on previously the cold air, there are better results in the inner defect (Group Two, Three and Four of Sample 1P), which benefits from this new variant, especially when replacing the vortex with the cooling fluid. Applying hot and cold flows at the same time tends to be the best

test across all groups. This technique also shows some advantages in inspecting curved samples and increasing the duration of exposure of the flows tends to boost the maximum temperatures of the defects, according to Group One of Sample 1P and samples 1C and 2. Debondings don’t benefit as much with this type of inspection as the delaminations and are greatly influenced by their position on the sample.

5 – RESULTS AND DISCUSSION OF ACU CHARACTERIZATION TESTS

5.1 – Introduction

This chapter describes the experiments made with the second NDT technique presented. This technique consists of an innovative variant of the Air-coupled Ultrasound, in which it is used the reflection mode instead of the conventional transmission mode. The goal of this chapter is to understand the effect of the parameters α, d and d_p, that enable the change of distance between the probes and the sample but at the same time, make sure there is reflection.

5.2 – ACU setup

In transmission mode, the inspection can be made with normal incidence, in the case of plain PLA samples, which means that between mediums air and PLA (Air / PLA), a part of the wave given by the transmitter probe is reflected (R1) and the remain is transmitted (T1), and between mediums PLA and Air (PLA / Air) some of T1 is reflected (R2) and the remain is transmitted to the receiver probe (T2). In this mode, when the wave

encounters a defect, the signal is mostly reflected to the receiver probe and so, the defect can be detected through the A-Scan because there's a change in signal amplitude.

However, in reflection mode, the inspection needs to be made with an angular incidence, to allow the wave to travel from the transmitter probe, reach the surface of the sample and reflect to reach the second probe. Therefore, the probes need to be set in a way that ensures this path of the wave. For the following experiments, there were studied three variables: α, d and d_p, and the first ones are bonded by a trigonometric relation, shown in Equation 5 and in Figure 5.1 b), in which *o* is 28.2 mm and is a fixed distance . This relation enables the change of distance between the probes and the sample but at the same time, always maintaining an angle that allows the wave to reach the sample and reflect. Distance d_p is the variable that reflects the change in distance across the Bosch Rexroth profile that bears the probes' support, without influencing α and d, as shown in Figure 5.1 a).

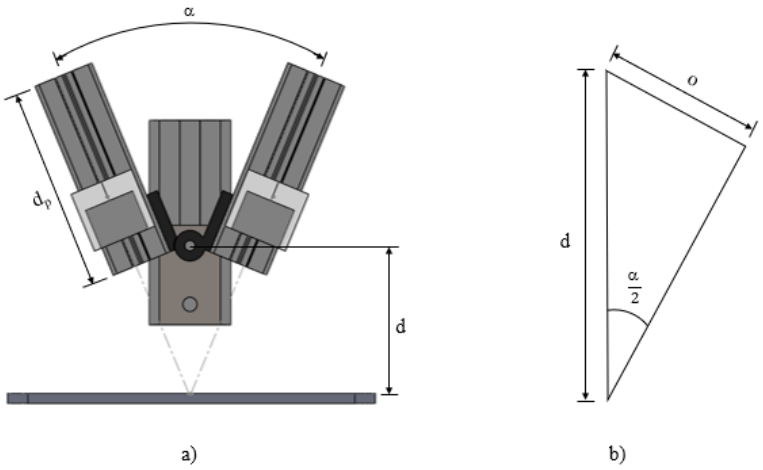

Figure 5.1 - Reflection mode set-up a) variables α, d and d_p b) relation between α and d.

$$d = \frac{o}{sen\left(\frac{\alpha}{2}\right)} \quad 5$$

Additionally, there are restrictions regarding the maximum and minimum values of α, d and d_p, due to the complete configuration of the inspection setup. The minimum and maximum distances of d that the assembled equipment allows between the sample and probes are 70 and 600 mm, respectively, the maximum distance of d_p is 68 mm and α can only vary between 5º and 55º. Having in mind these limitations and the trigonometric relation, there can be made several different inspections with different combinations of the variables, as presented in Table 5.1, *i.e.*, for α varying between 10º and 45º, d can

range between 73.6 and 323.1 mm. Additionally, d_p can vary between 0 and 60 mm for each value of d (and α) and so, the total number of possible configurations is 56.

Table 5.1 – Range of possible values for each variable.

α [º]	d [mm]	d_p [mm]
10	323,1	0
15	215,7	10
20	162,2	20
25	130,1	30
30	108,8	40
35	93,6	50
40	82,3	60
45	73,6	

5.3 – Sample Four inspection

For this sample, there were conducted two kinds of experiments, as shown in Figure 5.2:

- **Group One:** in these experiments, the face with the washer was on the same side of the probes;
- **Group Two:** in these experiments, the face with the washer was on the opposite side of the probes.

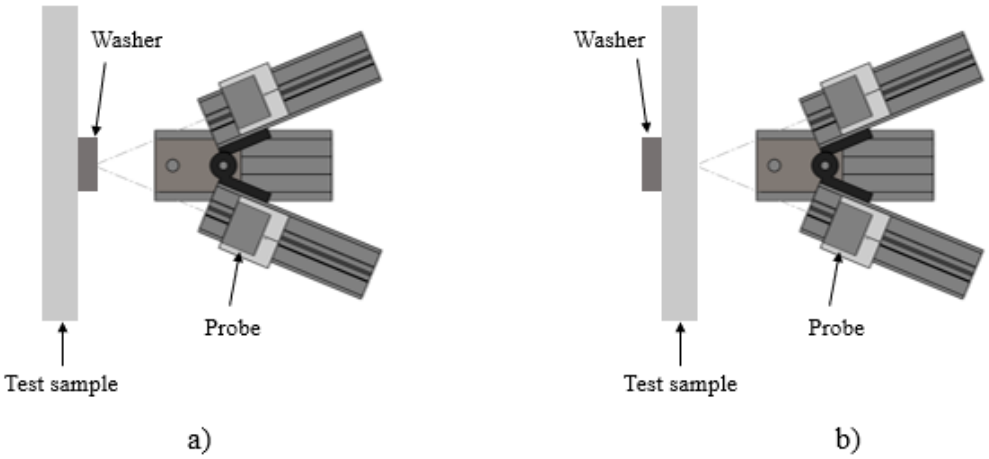

Figure 5.2 - Sample four experiments a) group one b) group two.

A stainless steel has a sound velocity of around 5800 m/s and an average density of 7740 kg/m^3, which means that its acoustic impedance Z is about 44.9x10^6 kg.m^{-2}.s^{-1}, which is 109067 times higher than air (411.6 kg.m^{-2}.s^{-1}) and 16 times higher than PLA (2.810^6 kg.m^{-2}.s^{-1}), and so a higher percentage of the wave will be reflected between Air / Metal and less will be transmitted between Metal / Air. This sample was inspected to begin to understand how the wave behaves in reflection mode configuration across different materials, especially the change in its amplitude, before inspecting samples with internal defects (Sample 3). The reason why there are two configurations for the washer is to understand the effect of α in the sample, if in reality, the transmission of the sound wave is being done across the probes onto the sample (and if so, it may be able to detect internal defects) and if it allows to detect different materials, even with a layer of PLA between the air and the metal (in Group Two).

5.3.1– Group One

In these experiments, there were conducted twenty-eight tests, whose values of d and d_p are displayed in Table 5.2 (in grey colour and with the legend of each experiment). These values of d were calculated based on the angles α but there are some which are very close to one another therefore not all the values were used in the experiments.

Table 5.2 - Experiments of Sample Four Group One.

d [mm]	d_p [mm]						
	0	10	20	30	40	50	60
215.7	d215dp0	d215dp10	d215dp20	d215dp30	d215dp40	d215dp50	d215dp60
130.1	d130dp0	d130dp10	d130dp20	d130dp30	d130dp40	d130dp50	d130dp60
82.3	d82dp0	d82dp10	d82dp20	d82dp30	d82dp40	d82dp50	d82dp60
73.6	d73dp0	d73dp10	d73dp20	d73dp30	d73dp40	d73dp50	d73dp60

For each experiment, it was collected three different echoes related with the three sample zones analysed, as shown in Figure 5.3, with a total of 84 different echoes.

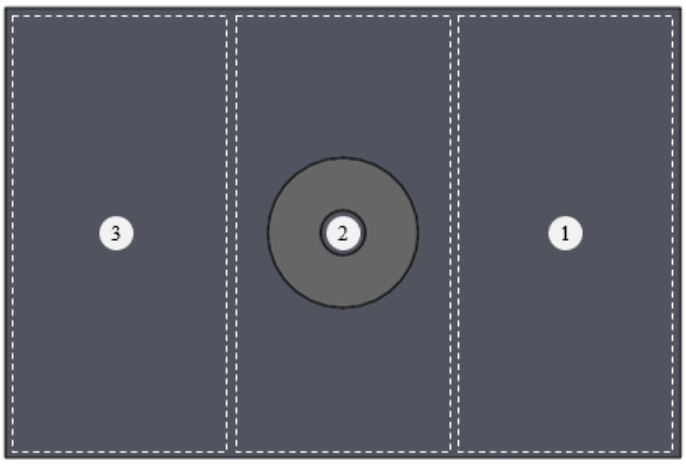

Figure 5.3 - Areas of sample four group one.

The images from Figure 5.4 show an example of one of the experiments (d=215.7 mm). The legend of each image, d(number)dp(number)_(number), indicates which values of d and d_p were used as well as which area, from Figure 5.3, does the echo belong to. For instance, the first image refers to the experiment where d=215.7 mm, d_p=0 mm and area 1.

These images are A-Scan representations of the amplitude of the sound wave received by the transmitter probe, in dB, as a function of the distance travelled by the wave, in mm. In the A-Scan, it can be retrieved, among other values, the space travelled by the wave, through the spatial scale; the percentage value of the maximum amplitude (inside the white box); the gain, in dB, and the step gate, which is 1 dB, in the upper right corner. For the experiments made in this chapter, the focus was to understand the change in amplitude, *i.e*. the intensity of the wave, through the step gate, when differing the variables, and whether it correlates with the density of the materials, and also to understand the echo of the reflected wave, how many echoes can be seen in the A-Scan in order to understand the distance where the sound was reflected and relate to the boundaries.

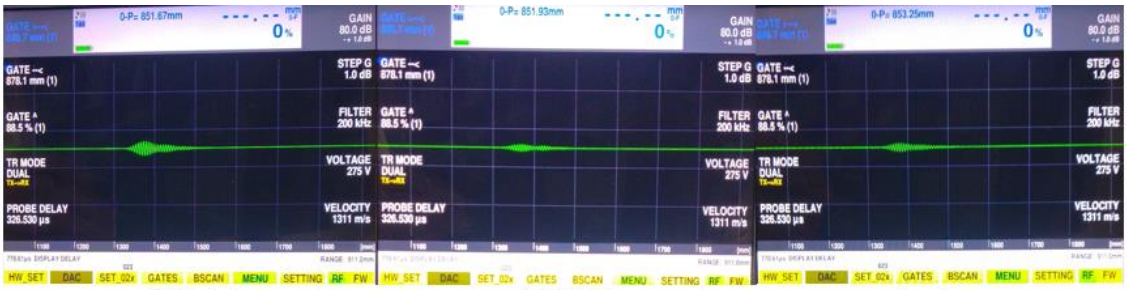

d215dp0_1 d215dp0_2 d215dp0_3

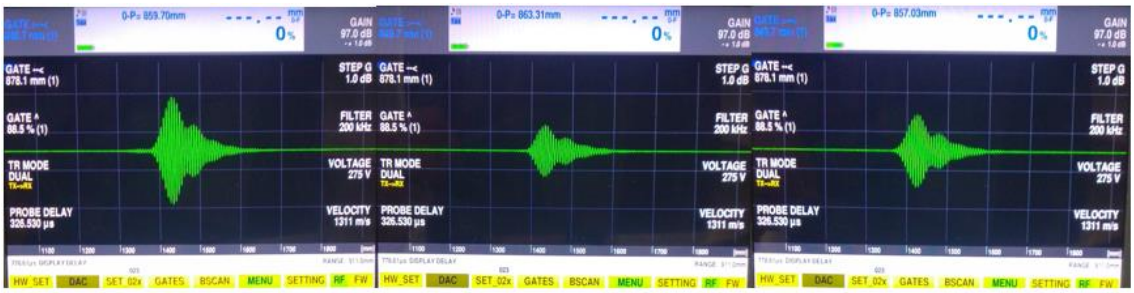

d215dp10_1 d215dp10_2 d215dp10_3

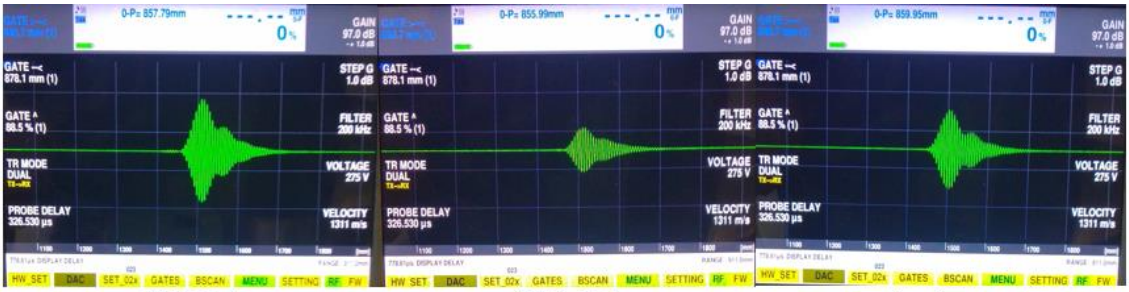

d215dp20_1 d215dp20_2 d215dp20_3

d215dp30_1 d215dp30_2 d215dp30_3

d215dp40_1 d215dp40_2 d215dp40_3

d215dp50_1 d215dp50_2 d215dp50_3

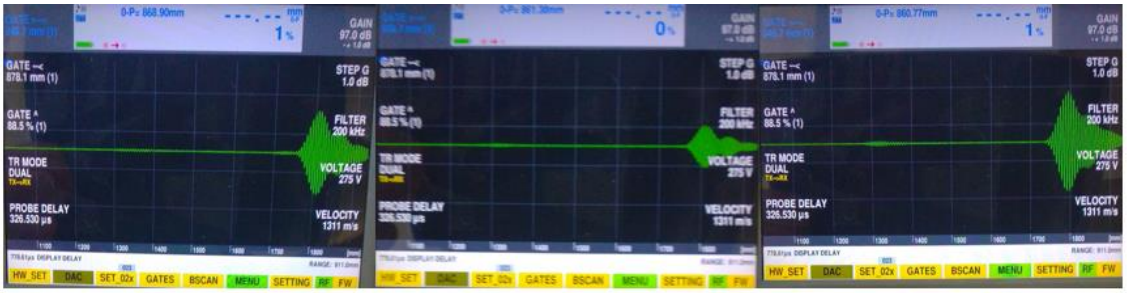

d215dp60_1 d215dp60_2 d215dp60_3

Figure 5.4 - Results of the experiment in which d=215.7 mm.

The results for all the 84 configurations show that the sound wave reflection echo is bigger in the PLA rather than in the washer even though, with the increase of d_p, there is a bigger reduction in the echo from the PLA than from the washer. Additionally, with the increase of d_p there is also an increase in the distance travelled by the waves, which is normal since the wave has a higher distance to travel to reach the sample and then the reflected wave has also more space to travel to reach the receiver probe. However, this increase in distance does not seem to decrease, in a linear way, the echo from the washer, according to the amplitude of the wave and the step gate.

With the increase of d, the amplitude of the echo decreases in all waves and there is the necessity of increasing the gain in order to better visualise the waves. With this increase there is also an increase in the distance travelled by the waves.

Since the metal is about 6 times denser than the PLA and with greater difference of Z, comparing with air, the reflected wave was expected to have more intensity than the one from the PLA, which does not happen. The reflected wave in all tests has only one echo, which means that the wave encountered only one boundary and then reflected, and whatever energy was transmitted (which was expected to be less due to the great difference of Z between Air / Metal and Air / PLA) was not reflected at the next boundary (Metal / PLA and PLA / Air) and received by the probe.

As distances d and d_p increase, the space with medium air that the wave has to travel becomes progressively bigger and because the acoustic attenuation of the air is higher than the one from PLA, the amplitude of the waves decrease through the tests.

5.3.2– Group Two

In these experiments, there were conducted ten tests, whose values of d and d_p are displayed in Table 5.3. Since in Group One, it was studied the effect of changing d_p into seven different values and it was understand, in some extent, the influence of the variable, in this group and in the following inspections, it is used only two values of d_p, 0 and 60 mm, which still allows to understand its effect, with five values of d.

Table 5.3 - Experiments of Sample four group two.

d [mm]	d_p [mm]	
	0	60
215.7	d215dp0	d215dp60
162.2	d162dp0	d162dp60
130.1	d130dp0	d130dp60
93.6	d93dp0	d93dp60
73.6	d73dp0	d73dp60

For each experiment, it was collected three different echoes related with the three sample zones analysed, as shown in Figure 5.5, with a total of 30 different echoes.

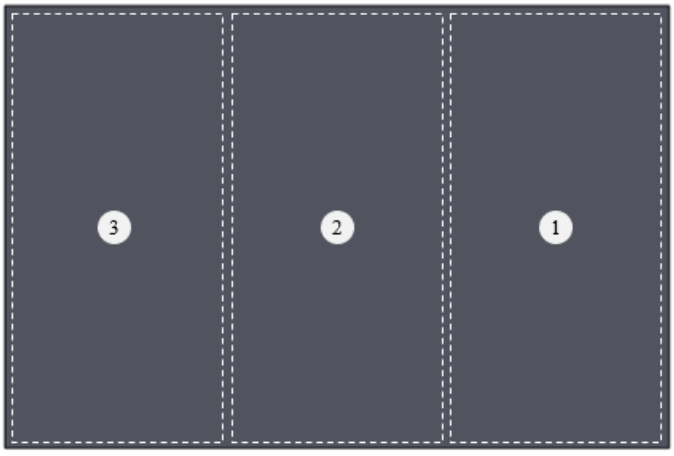

Figure 5.5 - Areas of sample four group two.

The images from Figure 5.6 show an example of one of the experiments (d=162.2 mm). The legend of each image, d(number)dp(number)_(number), indicates which values of d and d_p were used as well as which area, from Figure 5.5, does the echo belong to. For instance, the first image refers to the experiment where d=162.2 mm, d_p=0 mm and area 1.

These images are also A-Scan representations of the amplitude of the sound wave received by the transmitter probe, in dB, as a function of the distance travelled by the wave, in mm and the parameters inspected are the same as in Group One.

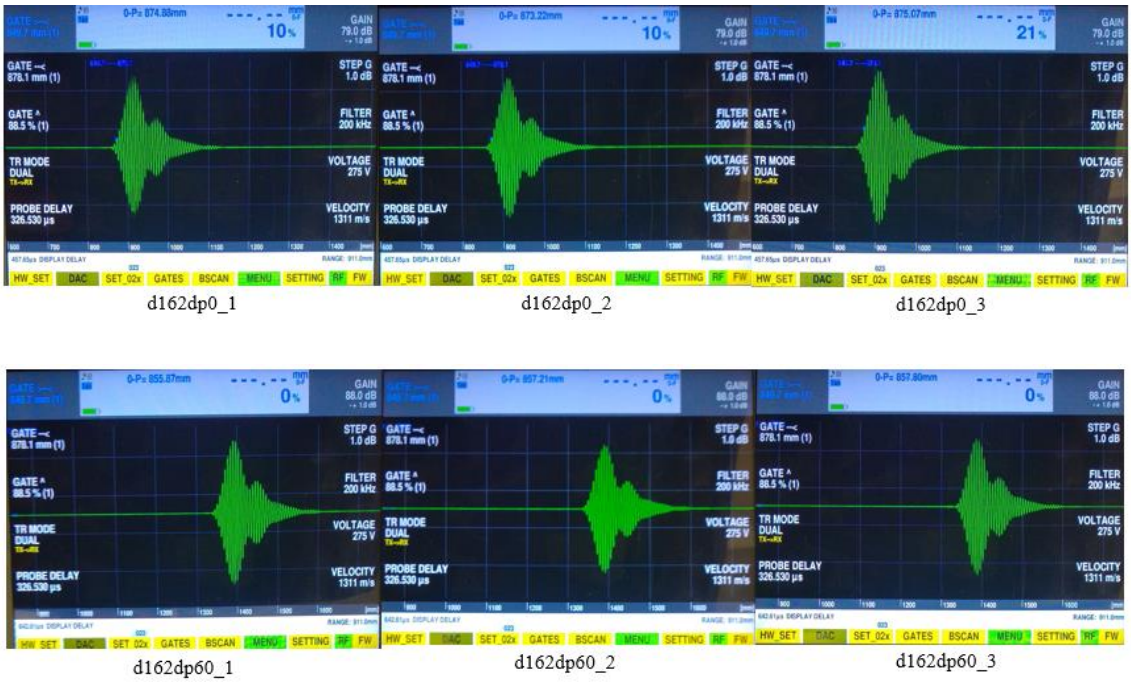

Figure 5.6 - Results of the experiment in which d=162.2 mm.

The results from all tests show that the amplitude of the sound wave was similar in both materials. With the increase of d_p and d there is a decrease in the echoes from the three areas and increase in the distance travelled by the waves (for the same reason as stated before, there's a bigger distance for the sound wave and reflected wave to travel). Additionally, with the increase of d, it's necessary to increase the gain in order to better visualise the waves (the intensity decreases with increasing distance). In some of the experiments, the echoes were bigger in area 3 compared to areas 1, although they are made from the same material, which can have happened due to some misplacement of the probes.

Since the amplitude of the echoes doesn't vary across the areas, the metal is not influencing the wave and so, in this configuration, and as concluded in Group One, what energy reaches subsequent boundaries and is reflected (if any) is not detected by the probe. All the more, the A-Scan presents only one echo, and so the wave encounters only one boundary.

5.4 – Sample Three inspection

For this sample, there were conducted ten reflection mode experiments, whose values of d and d_p are displayed in Table 5.3. The purpose of this experiment is to understand if this setup can identify internal defects. The results from Sample Four indicate that the wave does not reach the metal with the PLA in between nor indicate any boundary between Metal / Air (Sample Four Group One). This inspection serves to further assess whether some energy is transferred onto the PLA and if it reaches the defect, *i.e.* it is studied whether there is some delayed second echo, as the receiver probe receives the reflected energy.

For each experiment, it was collected three different echoes related with the three sample zones analysed, as shown in Figure 5.7, with a total of 30 different echoes.

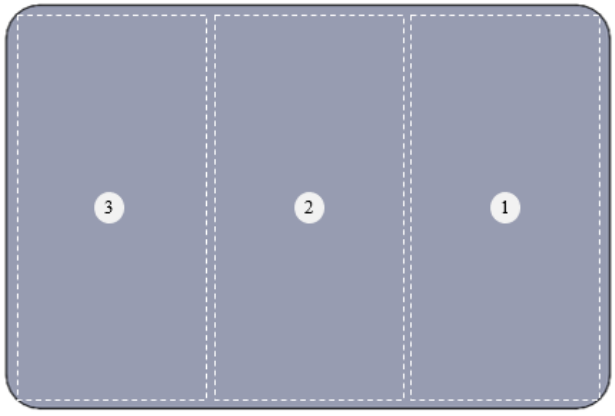

Figure 5.7 - Areas of sample three.

The images from Figure 5.8 show an example of one of the experiments (d=73.6 mm). The legend of each image, d(number)dp(number)_(number), indicates which values of d and d_p were used as well as which area, from Figure 6.7, does the echo belong to. For instance, the first image refers to the experiment where d=73.6 mm, d_p=0 mm and area 1.

These images are also A-Scan representations of the amplitude of the sound wave received by the transmitter probe, in dB, as a function of the distance travelled by the wave, in mm and the parameters inspected are the same as in Group One of Sample Four.

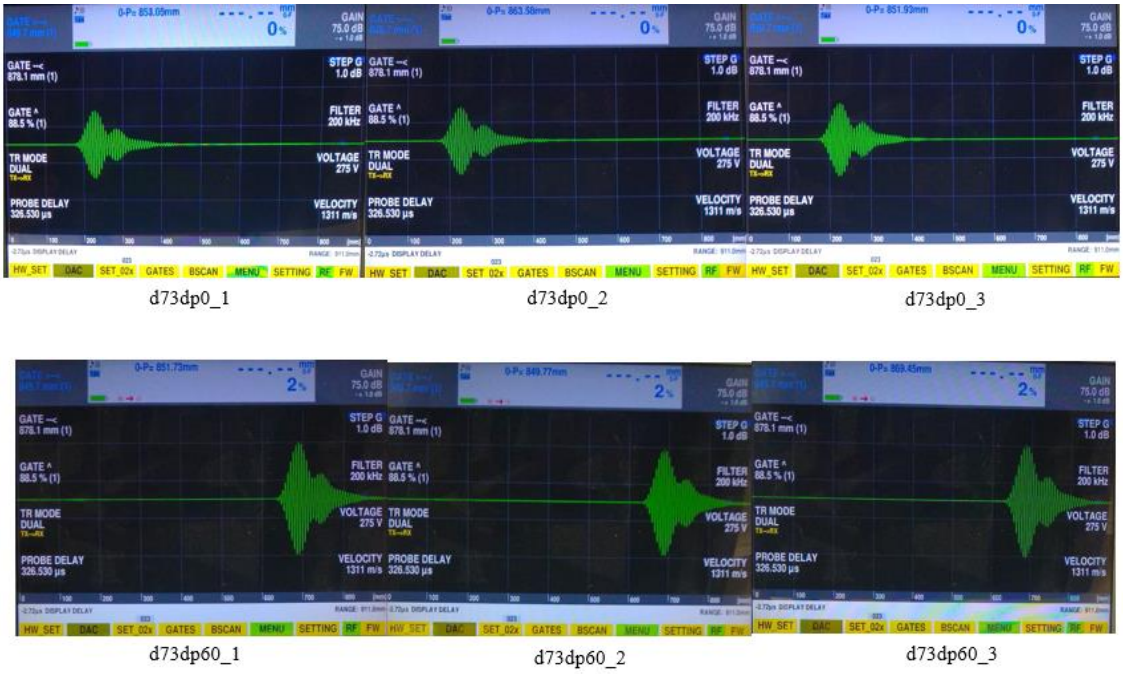

Figure 5.8 - Results of the experiment in which d=73.6 mm.

The results from all configurations show that there cannot be detected a difference of amplitudes between the echoes from the defect and free zone because the intensity, or amplitude of the wave, does not change across the areas. In area 2, there appears only one echo which means that the second probe is not receiving reflected energy from the defect inside the sample. Once again, with the increase of d_p and d there is a decrease in the echoes from the three areas and increase in the distance travelled by the waves.

In the first instance, these results and the ones from the previous sample indicate that this variant does not detect defects, or subsequent boundaries, as there is no second echo presented. But there is also an issue which may be jeopardizing the inspection: the position in which the sample was printed. Because this sample was not printed in the vertical position, the layers between the defect may have collapse during the printing operation, ceasing to exist a well-defined delamination inside the sample.

5.5 – Sample Five inspection

For this sample, there were conducted ten reflection mode experiments, whose values of d and d_p are displayed in Table 5.3. In the transmission mode, when comparing two samples, one thinner than the other, as the space of air that the wave has to travel is bigger in the first sample, the amplitude of the waves' echo is smaller (the acoustic attenuation coefficient of the air is bigger than the PLA one). In the reflection mode, the tests from the previous samples indicate the possibility of not being able to detect defects and that the expected behaviour of the echo with different materials is not proved by the results. The purpose of the following experiments was to understand the influence of differing the thickness when inspecting the same material (PLA).

For each experiment, it was collected three different echoes related with the three sample zones analysed, as shown in Figure 5.9, with a total of 30 different echoes.

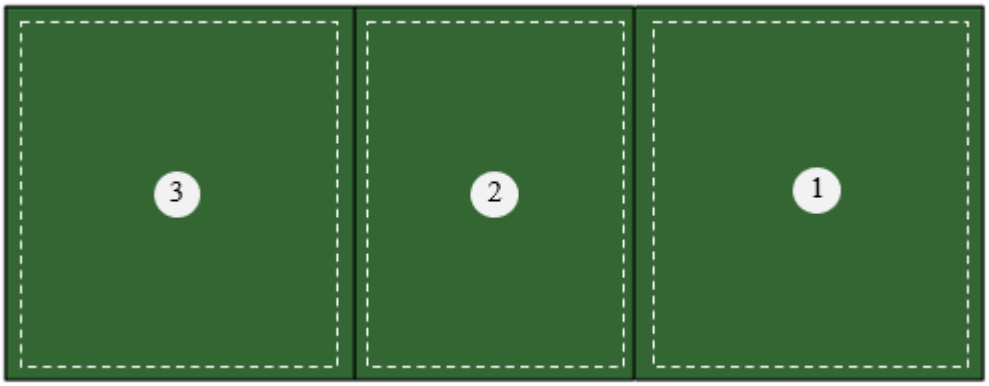

Figure 5.9 - Areas of sample three.

The images from Figure 5.10 show an example of one of the experiments (d=130.1 mm). The legend of each image, d(number)dp(number)_(number), indicates which values of d and d_p were used as well as which area, from Figure 5.9, does the echo belong to. For instance, the first image refers to the experiment where d=130.1 mm, d_p=0 mm and area 1. These images are A-Scans and were interpreted in the same way has the previous samples.

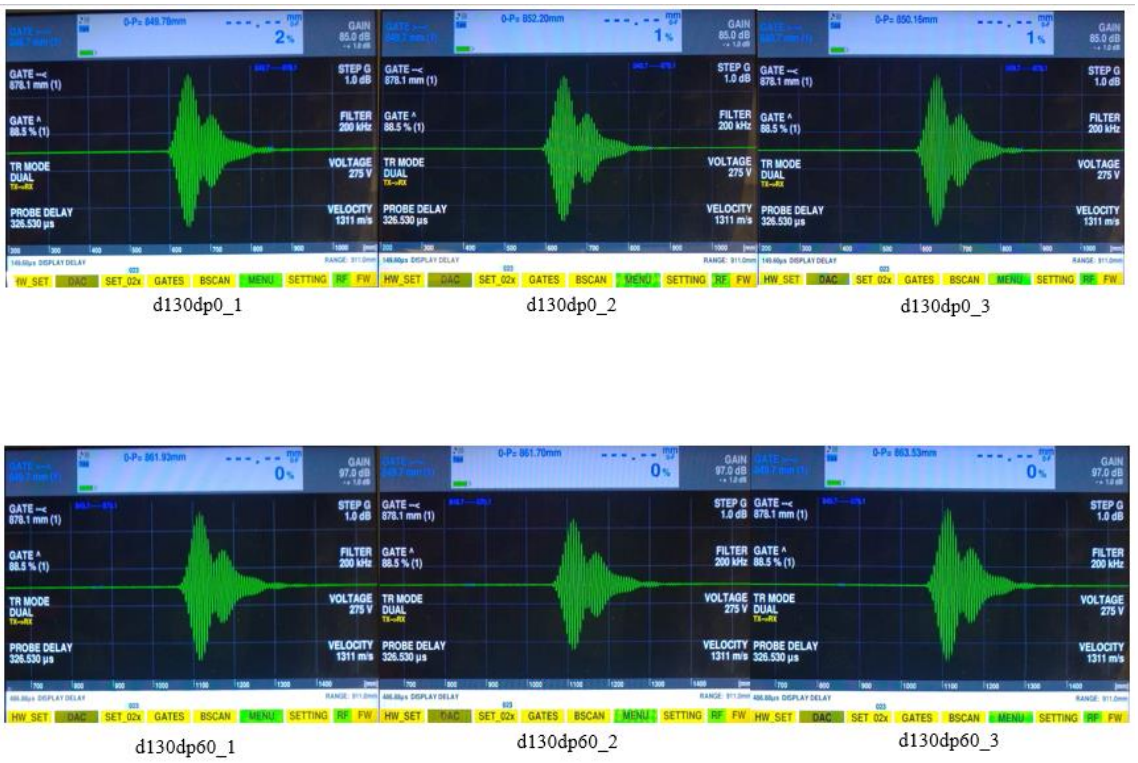

Figure 5.10 - Results of the experiment in which d=130.1 mm.

The results from the 30 inspections show that it is not detectable a difference of amplitudes between the echoes from areas 1 and 3, although their thickness are 2 and 4 mm, respectively. Area 2 tends to have a smaller echo. Once again, with the increase of d_p and d there is a decrease in the echoes from the three areas and increase in the distance travelled by the waves.

In area one, which has the smallest thickness, there's still one echo, reflecting the boundary Air / PLA as the only border encountered by the wave (Sample four has also a thickness of 2 mm and the same behaviour was observed). Since the density is the same across all areas, one explanation for the variation of the intensity of the echo in area 2 (which only happens in some tests) is due to some instability in the support where the probes where placed. With this group of tests, it seems that the variation of thickness of a sample is not detected with this technique.

5.6 – Chapter resume

This chapter describes the results and discussion of the three samples evaluated by the ACU NDT technique. The results show that this technique doesn't detect defects nor

variations in thickness across the sample, although other aspects, such as the quality of the sample and configuration/stability of the equipment should be taken into consideration. It is not clear the fractions of reflected and transmitted energy and some expected behaviour of the wave, especially its intensity regarding the different materials inspected (metal and PLA) was not backed up by the results.

6 – CONCLUSIONS AND SUGGESTIONS FOR FUTURE WORKS

6.1 – Conclusions

Regarding *Double Active Transient Thermography* (DATT), it can be concluded that the inner defect benefits more from the introduction of cold flow, whether the source is the vortex or the cooling fluid, although the latter provides 2.8 times better results and all defects have close contrast temperatures (between 3 and 5 ºC). For both sources, applying hot and cold flows simultaneously tends to provide the best results. In general, for this defect, these tests also provide better instants of maximum contrast.

In general, the outer defect does not benefit from the introduction of the cold since its maximum contrasts occurred near the end or immediately after the end of the hot flow and did not vary significantly across the tests.

The middle defect benefits, in some extent, from this technique: for most of the tests, the best contrasts were obtained with the presence of the cold, especially when applying both flows simultaneously. However, the difference between cold flow tests and reference was not so steep as with the inner defect.

Turning on previously the vortex proved to help the inner defect but not the outer and middle defects (as shown in Group Four and Three of Sample 1P). Using a lid which allows the recirculation of the air provides more stable evolutions of temperature but smaller temperature contrasts (from comparing the results of Group One and Two of Sample 1P), and influences the results and the tests that provide better contrasts.

Increasing the exposure time tends to increase the maximum contrast, which happens with Samples 1C, 2 and in Group One of Sample 1P (although this did not happen in the outer defect). The middle and inner defects of the curved sample also benefit from the introduction of the cold, applied alongside with the hot flow.

Regarding inspecting other defects other than delaminations, the debondings have almost 8 times less contrast than the delaminations and are greatly affected by their position when facing the hot flow. Finally, DATT tests showed that the technique allows a clearer observation of the three defects with different locations and depths at the same time, especially with cooling liquid.

In Air-coupled Ultrasound (ACU), the increase of distances d_p and d (following the reduction of α) causes a decrease in the amplitude of the sound's echo, due to the acoustic attenuation coefficient of air, and an increase in the distance travelled by the wave, because the wave and reflected wave have more space to travel to reach and come back from the sample.

The results show that some expected behaviour from the wave was not confirmed in the results, for example, since metal is denser than PLA, by inspecting this material, more energy would be reflected in the boundary between the Air / Material and more intensity would be shown in the A-Scan, which did not happen. In all results, only one echo appeared in the A-Scans, which indicates that this technique does not detect defects or subsequent boundaries that are not the border Air / Material. Moreover, the technique doesn't detect variations in thickness across the sample.

Despite these results, they do not prove the unsuitability of the technique, since it is not understood the behaviour of the wave with respect to its reflected and transmitted energies and other aspects, such as the quality of the sample and configuration/stability of the equipment, need to be taken into consideration and improved.

6.2 – Suggestions for future works

In future works, it is interesting to continue studying both techniques and deepen the knowledge regarding its capabilities. One thing that lacked in the present work was the repetition of tests in order to have a firmer idea of the advantages and disadvantages of each set of conditions and to avoid misunderstandings and doubts caused by the scattered data.

Furthermore, in DATT, it should be further studied the influence of exposure time; the conditions where defects from different locations and depths can be clearly seen at the same time, especially with the cooling liquid, and whether this technique is suitable and beneficial in inspecting curved surfaces, by carrying out many different inspections, as was done with sample 1P.

In ACU, it is interesting to further develop this technique, improving the equipment set up, using different probes and different samples, and to focus on understanding the behaviour of the sound wave and the path it travels from the transmitter probe to the receiver probe, including how much of the wave's energy is transmitted and reflected.

REFERENCES

[1] F. Ciampa, P. Mahmoodi, F. Pinto, M. Meo, Recent advances in active infrared thermography for non-destructive testing of aerospace components, Sensors (Switzerland). 18 (2018). https://doi.org/10.3390/s18020609.

[2] M.A. Machado, P.L. Inácio, R.A. Santos, A.F. Gomes, A.P. Martins, M.S. Carvalho, T.G. Santos, Inspection of composite parts produced by additive manufacturing: Air-coupled ultrasound and thermography, in: 58th Annu. Conf. Br. Inst. Non-Destructive Testing, NDT 2019, British Institute of Non-Destructive Testing, 2019.

[3] L.R. Sbriglia, A.M. Baker, J.M. Thompson, R. V. Morgan, A.J. Wachtor, J.D. Bernardin, Embedding sensors in FDM plastic parts during additive manufacturing, Conf. Proc. Soc. Exp. Mech. Ser. 10 (2016) 205–214. https://doi.org/10.1007/978-3-319-30249-2_17.

[4] P.M. Borba, A. Tedesco, D.M. Lenz, Effect of reinforcement nanoparticles addition on mechanical properties of SBS/curauá fiber composites, Mater. Res. 17 (2013) 412–419. https://doi.org/10.1590/s1516-14392013005000203.

[5] S. Guessasma, S. Belhabib, H. Nouri, Significance of pore percolation to drive anisotropic effects of 3D printed polymers revealed with X-ray μ-tomography and finite element computation, Polymer (Guildf). 81 (2015) 29–36. https://doi.org/10.1016/j.polymer.2015.10.041.

[6] S. Belhabib, W. Zhang, S. Guessasma, H. Nouri, J. Zhu, Challenges of additive manufacturing technologies from an optimisation perspective, Int. J. Simul. Multidiscip. Des. Optim. 6 (2016) A9. https://doi.org/10.1051/smdo/2016001.

[7] R. van Weeren, M. Agarwala, V.R. Jamalabad, A. Bandyophadyay, R. Vaidyanathan, N. Langrana, A. Safari, P. Whalen, S.C. Danforth, C. Ballard, Quality of Parts Processed by Fused Deposition, Solid Free. Fabr. (1995) 314–321.

[8] B.N. Turner, S.A. Gold, A review of melt extrusion additive manufacturing processes: II. Materials, dimensional accuracy, and surface roughness, Rapid Prototyp. J. 21 (2015) 250–261. https://doi.org/10.1108/RPJ-02-2013-0017.

[9] M. Ueda, A. Todoroki, Y. Hirano, M. Namiki, T. Nakamura, T.-K. Jeong, K. Horiguchi, R. Matsuzaki, H. Asahara, Three-dimensional printing of continuous-fiber composites by in-nozzle impregnation, Sci. Rep. 6 (2016). https://doi.org/10.1038/srep23058.

[10] Mukesh K. Agarwala, Vikram R. Jamalabad, Noshir A. Langrana, Ahmad Safari, Philip J. Whalen and, Stephen C. Danforth, Structural quality of parts processed by fused deposition, Rapid Prototyp. J. (1996).

[11] Vibrations and Ringing, (n.d.). https://www.simplify3d.com/support/print-quality-troubleshooting/vibrations-and-ringing/ (accessed July 19, 2020).

[12] T.-W.C. Z. Quan, A. Wu, M. Keefe, X. Qin, J. Yu, J. Suhr, J.-H. Byun, B.-S. Kim, Additive manufacturing of multi-directional preforms for composites: opportunities and challenges, Mater. Today. 18 (2015) 503–512.

[13] M.S. Carvalho, A.P. Martins, T.G. Santos, Simulation and validation of thermography inspection for components produced by additive manufacturing, Appl. Therm. Eng. 159 (2019) 113872. https://doi.org/10.1016/j.applthermaleng.2019.113872.

[14] S. Gholizadeh, A review of non-destructive testing methods of composite materials, in: Procedia Struct. Integr., Elsevier B.V., 2016: pp. 50–57. https://doi.org/10.1016/j.prostr.2016.02.008.

[15] M.A. Machado, L. Rosado, N. Pedrosa, R.M. Miranda, M. Piedade, T.G. Santos, Customized Eddy Current Probes for Pipe Inspection, Stud. Appl. Electromagn. Mech. 42 (2017) 283–290. https://doi.org/10.3233/978-1-61499-767-2-283.

[16] M.A. Machado, L. Rosado, N. Pedrosa, A. Vostner, R.M. Miranda, M. Piedade, T.G. Santos, Novel eddy current probes for pipes: Application in austenitic round-in-square profiles of ITER, NDT E Int. 87 (2017) 111–118. https://doi.org/10.1016/j.ndteint.2017.02.001.

[17] K.-N. Antin, M.A. Machado, T.G. Santos, P. Vilaça, Evaluation of Different Non-destructive Testing Methods to Detect Imperfections in Unidirectional Carbon Fiber Composite Ropes, J. Nondestruct. Eval. 38 (2019) 23. https://doi.org/10.1007/s10921-019-0564-y.

[18] M. Lizaranzu, A. Lario, A. Chiminelli, I. Amenabar, Non-destructive testing of composite materials by means of active thermography-based tools, Infrared Phys. Technol. 71 (2015) 113–120. https://doi.org/10.1016/j.infrared.2015.02.006.

[19] L. Lei, G. Ferrarini, A. Bortolin, G. Cadelano, P. Bison, X. Maldague, Thermography is cool: Defect detection using liquid nitrogen as a stimulus, NDT E Int. 102 (2019) 137–143. https://doi.org/10.1016/j.ndteint.2018.11.012.

[20] History of Composite Materials, Mar-Bal, Inc., (n.d.). https://www.mar-bal.com/applications/history-of-composites/ (accessed July 1, 2020).

[21] G. Schotte, A Brief History of Additive Manufacturing, TriMech Blog. (2019). https://blog.trimech.com/a-brief-history-of-additive-manufacturing (accessed July 1, 2020).

[22] History of Ultrasonics, (n.d.). https://www.nde-ed.org/EducationResources/CommunityCollege/Ultrasonics/Introduction/history.htm (accessed July 19, 2020).

[23] J.C.R. Granados, Detección y Reconstrucción de Defectos Subsuperficiales en 3-D mediante el Análisis de Datos de Termografía Pulsada, Centro de Investigaciones en Optica, A.C., 2011.

[24] R.M. Wang, S.R. Zheng, Y.P. Zheng, Polymer matrix composites and technology, 2011. https://doi.org/10.1533/9780857092229.

[25] M.A. Azmah Hanim, D. Brabazon, M.S.J. Hashmi, Cracks, microcracks, and fracture toughness of polymer composites, in: Fail. Anal. Biocomposites, Fibre-Reinforced Compos. Hybrid Compos., Elsevier, 2019: pp. 157–180. https://doi.org/10.1016/b978-0-08-102293-1.00008-5.

[26] D.D.L. Chung, Polymer-Matrix Composites: Structure and Processing, in: Carbon Compos., Elsevier, 2017: pp. 161–217. https://doi.org/10.1016/b978-0-12-804459-9.00003-8.

[27] P.K. Mallick, Thermoplastics and thermoplastic-matrix composites for lightweight automotive structures, in: Mater. Des. Manuf. Light. Veh., Elsevier Ltd., 2010: pp. 174–207. https://doi.org/10.1533/9781845697822.1.174.

[28] R.E. Shalin, ed., Polymer Matrix Composites, Springer Netherlands, Dordrecht, 1995. https://doi.org/10.1007/978-94-011-0515-6.

[29] R. Unnþórsson, M.T. Jonsson, T.P. Runarsson, NDT METHODS FOR EVALUATING CARBON FIBER COMPOSITES, n.d. www.weldtechnology.com (accessed January 5, 2020).

[30] B.P. Conner, G.P. Manogharan, A.N. Martof, L.M. Rodomsky, C.M. Rodomsky, D.C. Jordan, J.W. Limperos, Making sense of 3-D printing: Creating a map of additive

manufacturing products and services, Addit. Manuf. 1 (2014) 64–76. https://doi.org/10.1016/j.addma.2014.08.005.

[31] The 7 categories of Additive Manufacturing | Additive Manufacturing Research Group | Loughborough University, (n.d.). https://www.lboro.ac.uk/research/amrg/about/the7categoriesofadditivemanufacturing/ (accessed April 26, 2020).

[32] Standard Terminology for Additive Manufacturing Technologies, ASTM International (2012). https://doi.org/10.1520/F2792-12A (accessed November 23, 2019).

[33] Fused Deposition Modeling | FDM Printer & More - The Technology House, (n.d.). https://www.tth.com/3d-printing/fdm-prototyping/ (accessed July 10, 2020).

[34] I. Gibson, D. Rosen, B. Stucker, Additive manufacturing technologies: 3D printing, rapid prototyping, and direct digital manufacturing, second edition, 2015. https://doi.org/10.1007/978-1-4939-2113-3.

[35] D. Bourell, J.P. Kruth, M. Leu, G. Levy, D. Rosen, A.M. Beese, A. Clare, Materials for additive manufacturing, CIRP Ann. - Manuf. Technol. 66 (2017) 659–681. https://doi.org/10.1016/j.cirp.2017.05.009.

[36] D. Popescu, A. Zapciu, C. Amza, F. Baciu, R. Marinescu, FDM process parameters influence over the mechanical properties of polymer specimens: A review, Polym. Test. 69 (2018) 157–166. https://doi.org/10.1016/j.polymertesting.2018.05.020.

[37] O.A. Mohamed, S.H. Masood, J.L. Bhowmik, Analysis of wear behavior of additively manufactured PC-ABS parts, Mater. Lett. 230 (2018) 261–265. https://doi.org/10.1016/j.matlet.2018.07.139.

[38] X. Wang, M. Jiang, Z. Zhou, J. Gou, D. Hui, 3D printing of polymer matrix composites: A review and prospective, Compos. Part B Eng. 110 (2017) 442–458. https://doi.org/10.1016/j.compositesb.2016.11.034.

[39] B. Akhoundi, A.H. Behravesh, Effect of Filling Pattern on the Tensile and Flexural Mechanical Properties of FDM 3D Printed Products, Exp. Mech. 59 (2019) 883–897. https://doi.org/10.1007/s11340-018-00467-y.

[40] H.L. Brooks, A.E.W. Rennie, T.N. Abram, J. McGovern, F. Caron, Variable Fused Deposition Modelling - Analysis of benefits, concept design and tool path generation, in:

Innov. Dev. Virtual Phys. Prototyp. - Proc. 5th Int. Conf. Adv. Res. Rapid Prototyp., 2012: pp. 511–517. https://doi.org/10.1201/b11341-83.

[41] H. Bhavnagarwala, The Perfect ABS Print & Bed Temperature, All3DP. (2019). https://all3dp.com/2/abs-print-bed-temperature-all-you-need-to-know/ (accessed January 8, 2020).

[42] Díaz-García, J.Y. Law, A. Cota, A. Bellido-Correa, J. Ramírez-Rico, R. Schäfer, V. Franco, Novel procedure for laboratory scale production of composite functional filaments for additive manufacturing, Mater. Today Commun. 24 (2020). https://doi.org/10.1016/j.mtcomm.2020.101049.

[43] B. Chang, X. Li, P. Parandoush, S. Ruan, C. Shen, D. Lin, Additive manufacturing of continuous carbon fiber reinforced poly-ether-ether-ketone with ultrahigh mechanical properties, Polym. Test. 88 (2020). https://doi.org/10.1016/j.polymertesting.2020.106563.

[44] S. Kim, H. Wu, A. Devega, M. Sico, W. Fahy, J. Misasi, T. Dickens, J.H. Koo, Development of polyetherimide composites for use as 3D printed thermal protection material, J. Mater. Sci. 55 (2020) 9396–9413. https://doi.org/10.1007/s10853-020-04676-6.

[45] L.G. Blok, M.L. Longana, H. Yu, B.K.S. Woods, An investigation into 3D printing of fibre reinforced thermoplastic composites, Addit. Manuf. 22 (2018) 176–186. https://doi.org/10.1016/j.addma.2018.04.039.

[46] B. Brenken, E. Barocio, A. Favaloro, V. Kunc, R.B. Pipes, Fused filament fabrication of fiber-reinforced polymers: A review, Addit. Manuf. 21 (2018) 1–16. https://doi.org/10.1016/j.addma.2018.01.002.

[47] L. Trhlíková, O. Zmeskal, P. Psencik, P. Florian, Study of the thermal properties of filaments for 3D printing, in: AIP Conf. Proc., American Institute of Physics Inc., 2016. https://doi.org/10.1063/1.4955258.

[48] M. Wang, B. Gao, T. Wu, B. Hu, L. Liu, Defect depth retrieval method based on nonlinear transformation for pulsed thermographic inspection, Int. J. Therm. Sci. 149 (2020). https://doi.org/10.1016/j.ijthermalsci.2019.106196.

[49] Fluke Ti400 9hz Thermal Imager, (n.d.). https://www.myflukestore.com/p19040/fluke-flk-ti400-9hz-professional-320x240-thermal-imager-with-wireless-connectivity (accessed July 20, 2020).

[50] M. Koui, P. Theodorakeas, The use of pulsed thermography for the investigation of art and cultural heritage objects, in: 5th Int. Conf. NDT HSNT- IC MINDT, Eugenides Foundation, Athens, Greece, 2013.

[51] Thermography in the plastics industry | InfraTec, (n.d.). https://www.infratec.eu/thermography/industries-applications/plastics-industry/ (accessed December 27, 2019).

[52] Thermography in the aerospace industry | InfraTec, (n.d.). https://www.infratec.eu/thermography/industries-applications/aerospace-industry/ (accessed December 27, 2019).

[53] K.E. Cramer, Research Developments in Nondestructive Evaluation and Structural Health Monitoring for the Sustainment of Composite Aerospace Structures at NASA, 2016.

[54] V. Dattoma, R. Nobile, F.W. Panella, A. Saponaro, NDT thermographic techniques on CFRP structural components for aeronautical application, Procedia Struct. Integr. 8 (2018) 452–461. https://doi.org/10.1016/j.prostr.2017.12.045.

[55] P.D. Pastuszak, Characterization of Defects in Curved Composite Structures Using Active Infrared Thermography, in: Procedia Eng., Elsevier Ltd, 2016: pp. 325–332. https://doi.org/10.1016/j.proeng.2016.08.373.

[56] INTERNATIONAL ATOMIC ENERGY AGENCY, Non-destructive Testing: A Guidebook for Industrial Management and Quality Control Personnel, 1999.

[57] T.G. Santos, Seminar 3 - Ultrasonic Testing NDT, lecture notes, Advanced Manufacturing Processes and Non Destructive Testing 10514, Almada, 2019.

[58] Acoustic impedance and intensity: From Physclips Waves and Sound, (n.d.). https://www.animations.physics.unsw.edu.au/jw/sound-impedance-intensity.htm (accessed June 30, 2020).

[59] D. Tarrazó-Serrano, S. Castiñeira-Ibáñez, E. Sánchez-Aparisi, A. Uris, C. Rubio, MRI compatible planar material acoustic lenses, Appl. Sci. 8 (2018). https://doi.org/10.3390/app8122634.

[60] Light - Reflection and refraction | Britannica, (n.d.). https://www.britannica.com/science/light/Reflection-and-refraction (accessed January 5, 2020).

[61] Diffraction - Wave Behaviour RAFT, (n.d.). https://sites.google.com/site/wavebehaviourraft/diffraction (accessed January 5, 2020).

[62] Introduction to Ultrasonic Testing, (n.d.). https://www.nde-ed.org/EducationResources/CommunityCollege/Ultrasonics/Introduction/description.htm (accessed November 28, 2019).

[63] Air-coupled Ultrasound - A Millennial Review, (n.d.). https://www.ndt.net/article/wcndt00/papers/idn507/idn507.htm (accessed January 5, 2020).

[64] S. Joas, W. Essig, F. Fröhlich, M. Kreutzbruck, CFRP pipe inspection by means of air-coupled ultrasound, in: AIP Conf. Proc., American Institute of Physics Inc., 2019. https://doi.org/10.1063/1.5084893.

[65] W. Essiga, M. Kreutzbruck, Development of an inline monitoring system for quality assurance of thermoplastic CFRP tape using air-coupled ultrasound, in: AIP Conf. Proc., American Institute of Physics Inc., 2019. https://doi.org/10.1063/1.5121677.

[66] J. Neuenschwander, R. Furrer, A. Roemmeler, Application of air-coupled ultrasonics for the characterization of polymer and polymer-matrix composite samples, Polym. Test. 56 (2016) 379–386. https://doi.org/10.1016/j.polymertesting.2016.11.002.

[67] Fluke Ti400 Infrared Camera With Fluke Connect | Fluke, (n.d.). https://www.fluke.com/en-us/product/thermal-cameras/ti400 (accessed July 20, 2020).

[68] DIO 1000 LF - STARMANS, (n.d.). http://www.starmans.net/product/dio-1000-lf/ (accessed March 22, 2020).

[69] Sci-Hub | Surface wave techniques for evaluation of concrete structures. Non-Destructive Evaluation of Reinforced Concrete Structures, 441–465 | 10.1533/9781845699604.2.441, (n.d.). https://sci-hub.se/10.1533/9781845699604.2.441 (accessed November 28, 2019).

[70] S. Jones, Ground vibration from underground railways: how simplifying assumptions limit prediction accuracy, (2010). https://www.researchgate.net/publication/280986859_Ground_vibration_from_underground_railways_how_simplifying_assumptions_limit_prediction_accuracy (accessed January 5, 2020).

[71] Lamb Wave Generation, (n.d.). https://www.nde-

ed.org/EducationResources/CommunityCollege/Ultrasonics/EquipmentTrans/ematlambwave.htm (accessed January 5, 2020).

APPENDIX

Appendix 1. Common matrix materials and its properties

- **Polytetrafluoroethylene (PTFE)** or Teflon® (the registered trade name) belongs to the class of plastics fluoropolymer and is the polymerized form of tetrafluoroethylene (TFE). It is used for coating machine parts, cookware, laboratory equipment and communication cables, among others, due to its high melting point, stability at very low temperatures, resistance to corrosion, low electrical conductivity and low friction;
- **Polyamide (PA)** are polymers containing repeating amide linkages. The type of PA most used in matrix materials are aliphatic polyamides, known as Nylon® (the registered trade name), that have high tensile strength, higher toughness and resistance to abrasion as well as other properties, such as the ability to absorb water (PA6.6) and enhanced elasticity (PA6). As example, they are used in battery casings, brake hoses and for footwear;
- **Polylactic Acid (PLA)** is a biodegradable thermoplastic polyester derived from biomass and it's widely used, for example, in Fused Filament Fabrication machines, due to its ability to be reheated to its melting point and cooled without significant deterioration, and the fact that it naturally degrades, in the solid form, when exposed to the environment;
- **Acrylonitrile Butadiene Styrene (ABS)** is an amorphous thermoplastic polymer used for injection moulding processes and prototyping materials because it's easy to manufacture, has low melting temperature, and endures corrosive chemicals and physical impacts.
- **Polyetherimide (PEI)** or Ultem® (the registered trade name) is an amorphous thermoplastic used in internal components of microwave ovens, electronic products, and in transportation applications, among others, because of features like its high strength and modulus, good electrical properties and flame and heat endurance;
- **Polyetheretherketone (PEEK)** is a recycling plastic belonging to the family of polyketone and is used in fields like aerospace, automobile and biomedical because of its high performance, high temperature resistance, long-term corrosion resistance, low friction, good dimensional stability and biocompatibility;

- **Polycarbonate (PC)** is an amorphous thermoplastic created from Bisphenol A (BPA) and used for transparency products, plastic lenses in eyewear, medical devices, Digital Disks, such as CDs and DVDs, due to its impact and heat resistance, among other features;
- **Epoxy** is a resin, also created from Bisphenol A (BPA) and an epoxide that is used as adhesives, surface coatings and food containers.

Appendix 2. Two modes of wave propagation in solids

- **Rayleigh waves**, which is a surface wave that combines longitudinal and transverse move to create an elliptical motion, moving along a free surface or the boundary between mediums. They are very sensitive to surface defects and follow the surface around curves;
- **Lamb waves**, which is an elastic wave and a type of Plate waves, where its oscillation lies in a plane that contains both the trajectory direction and the direction perpendicular (its normal) [69].

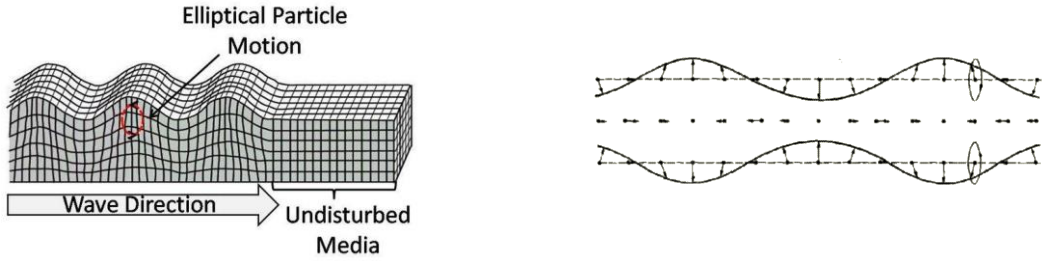

a) b)

Figure A1 - Schematic representation of a) Rayleigh wave [70] b) Lamb wave [71].